

Sensitivity of Polarization to Grain Shape: II. AggregatesB. T. DRAINE^{1,2}¹*Dept. of Astrophysical Sciences, Princeton University, Princeton, NJ 08544, USA*²*Institute for Advanced Study, Princeton, NJ 08540, USA*

ABSTRACT

A previous study (Paper I) investigated the polarization properties of a variety of simple convex grain shapes, some of which were found to be consistent with the observed polarization properties of interstellar dust from far-ultraviolet to far-infrared. Here we study the optical properties of 45 non-convex shapes, all aggregates of N equal-sized spheres. We consider $N = 2$, $N = 3$, and $N = 256$ random aggregates obtained from 3 different aggregation schemes. We also consider “trimmed” $N = 256$ aggregates obtained by systematically trimming initially random aggregates to increase either flattening or elongation. The “macroporosities” of the studied aggregates range from $\mathcal{P}_{\text{macro}} = 0.18$ (for the $N = 2$ bisphere) to $\mathcal{P}_{\text{macro}} \approx 0.85$ (for the $N = 256$ “BA” aggregates). The only aggregates consistent with observations of starlight polarization and polarized thermal emission are shapes that have been trimmed to increase their asymmetry. If interstellar grains are high-porosity aggregates, there must be processes causing extreme elongation or flattening; if not, interstellar grains must be dominated by fairly compact structures, with at most moderate porosities. The ratio of polarization in the $10\mu\text{m}$ silicate feature to starlight polarization in the optical is shown to be insensitive to porosity and shape. X-ray scattering may be the best tool to determine the porosity of interstellar grains. We propose that modest porosities of interstellar grains could be the result of “photolytic densification”. High polarization fractions observed in some Class-0 cores require processes to reduce porosities and/or increase asymmetries of aggregates in dense regions.

Keywords: interstellar dust (836), radiative transfer (1335)

1. INTRODUCTION

Interstellar dust obscures and reddens stars, emission nebulae, and active galactic nuclei, and adds “foreground” emission to the cosmic microwave background. The need to correct for these effects has provided motivation for continuing efforts to improve our understanding of interstellar dust.

In addition, it is now recognized that interstellar dust directly affects the dynamics of the interstellar medium, and thereby the structure and evolution of star-forming galaxies. The shielding effects of dust permit molecules to survive; catalysis of molecular hydrogen on grain surfaces initiates most interstellar chemistry; photoelectrons from dust grains heat the interstellar medium; recombination of ions and electrons on grain surfaces lowers the degree of ionization in predominantly neutral regions; charged dust grains help to couple neutral gas to the magnetic field; and radiation pressure acting on dust can be dynamically important for interstellar gas.

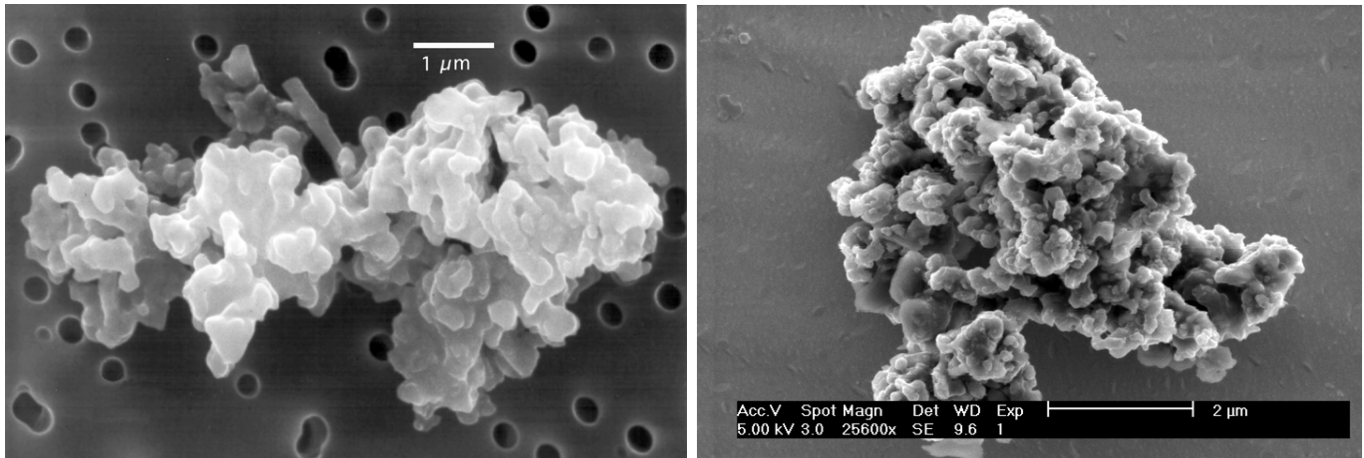


Figure 1. Two porous-chondrite interplanetary dust particles. Left: Credit Don Brownlee (U. Washington). Right: Credit Nicole Spring (U. Manchester) and Henner Busemann (ETH Zurich).

Dust is also valuable as a *diagnostic* of the interstellar medium – the spectrum of infrared emission from the dust informs us of the intensity of starlight heating the dust, the polarization of starlight and the polarized thermal emission from dust reveals the ordering of the interstellar magnetic field. Finally, the abundance, composition, and size distribution of dust grains have much to tell us of the history of the interstellar medium within which grains are grown, shattered, and sputtered. Every grain is itself a historical record, if only we knew how to read it.

Despite the astrophysical importance of interstellar dust, there remain substantial uncertainties regarding the chemical composition and morphology of the dust grains.

It is often suggested that interstellar grains are high-porosity structures – sometimes characterized as “fluffy” – formed by aggregation of smaller particles. Interplanetary dust particles (IDPs) – thought to originate in comets, and collected in the stratosphere – often have this geometry (Bradley 2003). The most common type of IDPs linked to short-period comets are the “anhydrous chondritic-porous IDPs” (see Figure 1). These have a substantial silicate component, a carbonaceous matrix, and a porous structure (Keller & Messenger 2005). The IDPs in Figure 1 are much larger than the typical submicron interstellar dust particle, but demonstrate that high-porosity aggregate structures are present in some astrophysical settings.

High porosity (vacuum fraction) has also been invoked to explain polarized scattered light from particles in the AU Mic debris disk; these particles may resemble the IDPs in our solar system. Graham et al. (2007) argued for porosities as high as $\mathcal{P} = 0.91 - 0.94$; Shen et al. (2009) later showed that light scattering by the AU Mic debris disk is consistent with more modest grain porosities, $\mathcal{P} \approx 0.6$.

The emission spectra of protoplanetary disks have been interpreted as indicative of grain growth to mm or even cm sizes (Beckwith & Sargent 1991; Testi et al. 2003; Draine 2006). Polarized emission from the HL Tau protoplanetary disk was modeled by Zhang et al. (2023) using mm-sized particles with high porosities, $\mathcal{P} \approx 0.70 - 0.97$.

High porosities have also been proposed for submicron-sized interstellar grains. Mathis (1996) suggested that porosity could alleviate perceived stress between the observed extinction of starlight, and the available abundances of dust-forming elements such as C and Si, the idea being that the increased surface area of fluffy grains might result in increased extinction cross section per unit mass. However, Dwek (1997) and Li (2005) later concluded that increasing porosity doesn’t actually reduce the mass in grains required to account for the observed extinction.

High porosities have been invoked to help explain the relatively high far-infrared (FIR) and submm opacities of interstellar dust. Mathis & Whiffen (1989) argued that interstellar grains with sizes

$\gtrsim 0.01\mu\text{m}$ are composites, with porosity $\mathcal{P} \approx 0.8$. Voshchinnikov et al. (2006) proposed models with porosities ranging from $\mathcal{P} = 0.90$ to 0.98 . Hirashita et al. (2021) argued that interstellar particles larger than $\sim 0.1\mu\text{m}$ should have porosities $\mathcal{P} > 0.7$.

Despite the numerous papers arguing that interstellar grains have high porosity, it is not clear that such high-porosity grains are consistent with the observed properties of interstellar dust. Heng & Draine (2009) argued that the X-ray scattering halo observed around GX13+1 required *low* porosities $\mathcal{P} \lesssim 0.55$ to match the angular profile of the halo.

In the present work we ask whether high-porosity grains are consistent with the observed polarizing properties of interstellar dust. The polarizing efficiency of interstellar dust is observed to be quite high; this strongly constrains the shapes of interstellar dust grains (Rogers & Martin 1979; Kim & Martin 1995; Draine & Fraise 2009; Fanciullo et al. 2017; Draine & Hensley 2021a; Hensley & Draine 2023; Ysard et al. 2024). Paper I (Draine 2024) considered a variety of simple convex shapes. Some of the considered shapes were found to be consistent with the observed polarization of starlight and polarized FIR emission, whereas certain other shapes could be ruled out.

The present work extends this study to a variety of non-convex grain shapes formed by aggregation of spheres, resulting in irregular structures with substantial “macroporosity”. Using the discrete dipole approximation (DDA), we calculate scattering and absorption cross sections for complex grain geometries over a wavelength range running from the far-ultraviolet (FUV) to the FIR. The polarizing properties of aligned grains with these shapes are compared to the observed polarization of starlight and polarized FIR emission from aligned dust grains. We find that many of the considered porous geometries can be ruled out because they are incapable of reproducing the polarizations observed on some interstellar sightlines *even if the $a \gtrsim 0.1\mu\text{m}$ grains are in “perfect spinning alignment” (PSA)*. We conclude that the $0.1\text{--}0.3\mu\text{m}$ grains primarily responsible for the observed polarization of starlight are not produced by random aggregation alone. However, we show that porous aggregates are allowed, provided that they are “trimmed” to have extreme flattenings or elongations. Examples of such aggregates are presented.

Section 2 discusses quantitative measures of porosity and overall asymmetry of individual grains, and section 3 presents the considered grain geometries. Section 4 describes the methodology for calculating optical cross sections; calculated cross sections are presented in Section 5. Section 6 discusses the effective wavelength λ_p for polarization as a function of grain size and shape, as well as the dimensionless width σ_p of the polarization profile. For each considered shape, the starlight polarization efficiency integral Φ_{PSA} is calculated in Section 7. Section 8 presents the polarizing properties of the grains near the $10\mu\text{m}$ silicate feature, and in the FIR.

The results are discussed in Section 9, and summarized in Section 10.

2. ASYMMETRY AND POROSITY

The optical properties of a grain depend on composition, size, and – particularly for polarized extinction and emission – on the grain shape. The size of an irregular particle can be characterized by the “mass-equivalent” effective radius

$$a_{\text{eff}} \equiv \left(\frac{3M}{4\pi\rho_{\text{solid}}} \right)^{1/3}, \quad (1)$$

where M is the mass, and ρ_{solid} is the mass density of the solid material.

The grain has moments of inertia $I_1 \geq I_2 \geq I_3$ for rotation around each of the principal axes, $\hat{\mathbf{a}}_1, \hat{\mathbf{a}}_2, \hat{\mathbf{a}}_3$. Let

$$\alpha_j \equiv \frac{I_j}{0.4Ma_{\text{eff}}^2}, \quad j = 1, 2, 3 \quad . \quad (2)$$

A sphere has $\alpha_1 = \alpha_2 = \alpha_3 = 1$.

Let $\mathbf{r} = x\hat{\mathbf{a}}_1 + y\hat{\mathbf{a}}_2 + z\hat{\mathbf{a}}_3$, with the center of mass at $\mathbf{r} = 0$. For any given shape, the dimensionless α_j can be used to define an asymmetry parameter

$$\mathcal{A} \equiv \left(\frac{\langle y^2 \rangle + \langle z^2 \rangle}{2\langle x^2 \rangle} \right)^{1/2} = \left(\frac{\alpha_1}{\alpha_2 + \alpha_3 - \alpha_1} \right)^{1/2}. \quad (3)$$

A sphere has $\mathcal{A} = 1$; elongated or flattened shapes have $\mathcal{A} > 1$.¹

We distinguish between “microporosity” $\mathcal{P}_{\text{micro}}$ – due to voids and defects on atomic scales² – and “macroporosity” $\mathcal{P}_{\text{macro}}$, characterizing the presence of voids on scales much larger than the interatomic separation.

A number of different approaches have been taken to quantify the macroporosity of irregular grains. Mukai et al. (1992) set $\mathcal{P}_{\text{M92}} = 1 - V_{\text{solid}}/V_{\text{M92}}$, where V_{M92} is the volume of a sphere with the same radius of gyration. Note that with this definition a solid spheroid or ellipsoid, by virtue of being nonspherical, would have $\mathcal{P}_{\text{M92}} > 0$, even though the actual macroporosity is zero. Ossenkopf (1993) used the angle-averaged projected area to define a “fluffiness parameter”.

In the present work we employ the macroporosity defined by Shen et al. (2008):

$$\mathcal{P}_{\text{macro}} \equiv 1 - \frac{V_{\text{solid}}}{V_{\text{S08}}} \equiv 1 - \frac{1}{[(\alpha_2 + \alpha_3 - \alpha_1)(\alpha_3 + \alpha_1 - \alpha_2)(\alpha_1 + \alpha_2 - \alpha_3)]^{1/2}}, \quad (4)$$

where V_{S08} is the volume of an ellipsoid with the same I_j/M as the grain. With this definition, solid spheres, spheroids, and ellipsoids have $\mathcal{P}_{\text{macro}} = 0$, as desired.³

Ellipsoidal aggregates formed from N close-packed single-size spheres have $\mathcal{P}_{\text{macro}} = 1 - \pi/(3\sqrt{2}) = 0.2595\dots$ for $N \rightarrow \infty$ (Gauss 1831). Depending on the growth process, random aggregates can have values of $\mathcal{P}_{\text{macro}}$ approaching unity [e.g., random aggregates formed by “diffusion limited aggregation” (Witten & Cates 1986)].

If the grain material has “microporosity” $\mathcal{P}_{\text{micro}}$ and the shape has macroporosity $\mathcal{P}_{\text{macro}}$, the total porosity is

$$\mathcal{P} = 1 - (1 - \mathcal{P}_{\text{micro}})(1 - \mathcal{P}_{\text{macro}}) \quad . \quad (5)$$

3. AGGREGATES

Aggregation of dust grains is expected to occur in the interstellar medium, and to play an important role in the evolution of distribution of grain sizes. Aggregation is also expected to result in porous grains.

Grain models that reproduce the observed interstellar extinction curve typically have most of the grain mass in grains with $a_{\text{eff}} \gtrsim 0.05\mu\text{m}$,⁴ but with smaller grains still accounting for an appreciable fraction of the mass, and greatly outnumbering the larger grains. The larger aggregates likely contain subunits (“monomers”) spanning a range of sizes.

The objective of the present work is to study the polarization properties of porous aggregates. We do not consider that the details of the aggregate geometry are realistic – only that they span an interesting range of porosities. To this end, we investigate aggregates of N equal-sized spherical monomers. We limit study to aggregates of equal-size spheres for simplicity, and for computational

¹ Note that \mathcal{A} defined by Eq. (3) differs from the parameter $\mathcal{A}' = \alpha_1/(\alpha_2\alpha_3)^{1/2}$ defined in Paper I (Draine 2024, Eq. 2). We find that \mathcal{A} defined by (3) is a better predictor of polarizing properties of irregular grains than \mathcal{A}' .

² Normal polycrystalline materials have some level of microporosity. If the ideal mineral has density ρ_c , but a solid sample with the same chemical composition has density ρ_{solid} , we define the microporosity to be $\mathcal{P}_{\text{micro}} = 1 - \rho_{\text{solid}}/\rho_c$. For example, in both graphite and glassy carbon $\sim 100\%$ of the C atoms are thought to be in sites with sp^2 bonding (Robertson 1986); however, crystalline graphite has $\rho_c = 2.26\text{ g cm}^{-3}$, whereas “glassy carbon” samples have $\rho_{\text{solid}} = 1.3 - 1.55\text{ g cm}^{-3}$, corresponding to $\mathcal{P}_{\text{micro}} = 0.31 - 0.43$. “Pyrolytic graphite” has $\rho_{\text{solid}} = 1.22 - 2.22\text{ g cm}^{-3}$ for production temperatures 1900 – 2400 K (Yajima et al. 1965), corresponding to $\mathcal{P}_{\text{micro}} = 0.02 - 0.46$.

³ Note, however, that non-ellipsoidal solids have $\mathcal{P}_{\text{macro}} > 0$; for example, cylinders have $\mathcal{P}_{\text{macro}} = 0.070$, and rectangular prisms have $\mathcal{P}_{\text{macro}} = 0.112$.

⁴ E.g., the MRN size distribution (Mathis et al. 1977) has 64% of the mass in grains with $0.05\mu\text{m} < a < 0.25\mu\text{m}$.

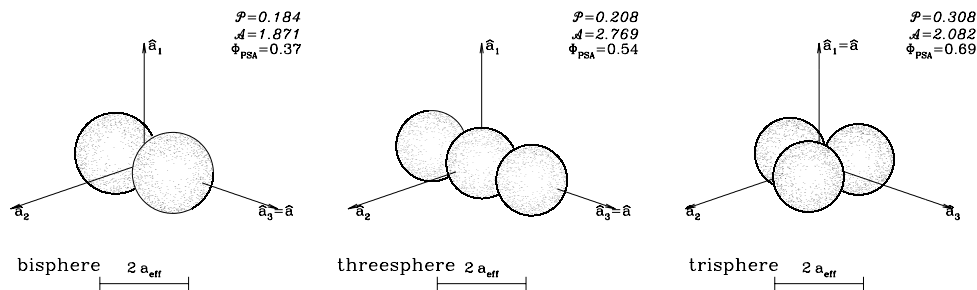


Figure 2. Bisphere, threesphere, and trisphere geometries. The scale bars show $2a_{\text{eff}}$, the diameter of an equal-volume sphere. \hat{a}_1 is the principal axis of largest moment of inertia; grains are assumed to spin around this axis.

feasibility. We study the cases of $N = 2$ and $N = 3$, but most of the study concerns $N = 256$ aggregates resulting from different aggregation schemes, with macroporosities $\mathcal{P}_{\text{macro}}$ ranging from ~ 0.53 to ~ 0.85 .

Aggregates incorporating a wide range of monomer sizes would be more realistic than assuming equal-size monomers: the smaller particles may tend to fill in the spaces between the larger particles, lowering the porosity, although this will depend on the assumed dynamics of aggregation. For the results to be accurate, DDA calculations of scattering and absorption by aggregates require that each monomer be represented by a sufficient number of dipoles that the shape of its surface is adequately emulated. If the smallest monomers are allowed to be very small (by volume) compared to the overall aggregate, the overall number of dipoles required quickly becomes computationally prohibitive.

While recognizing the greater realism of aggregates of polydisperse monomers, we defer their investigation to future work, here limiting study to aggregates of equal-size spheres.

3.1. $N = 2$ and $N = 3$ Aggregates

There is only one structure consisting of two equal-sized touching spheres:

- **“bisphere”**: 2 touching spheres, with $\mathcal{P}_{\text{macro}} = 0.184$, and asymmetry factor $\mathcal{A} = 1.871$.

We consider 2 examples of structures made up of 3 equal-size spheres:

- **“threesphere”**: 3 collinear touching spheres, with $\mathcal{P}_{\text{macro}} = 0.208$, and $\mathcal{A} = 2.769$.
- **“trisphere”**: 3 touching spheres in close-packed geometry, with $\mathcal{P}_{\text{macro}} = 0.308$, and $\mathcal{A} = 2.082$.

These simple shapes are shown in Figure 2. Geometric parameters are given in Table 1.

3.2. $N = 256$ Random Aggregates

We also consider irregular structures comprised of $N = 256$ equal-size spheres, created following three different growth rules described by Shen et al. (2008): A library of BA, BAM1, and BAM2 aggregates, including the examples studied here, can be found at www.astro.princeton.edu/~draine/agglom.html.

- **BA** (“Ballistic Aggregation”, also known as “Particle-Cluster Aggregation”): Spherical monomers arrive on random trajectories, and stick wherever they first touch. This growth scheme creates high-porosity structures. For $N = 256$, BA aggregates have $\mathcal{P}_{\text{macro}} \approx 0.847 \pm 0.013$ (Shen et al. 2008, the “uncertainty” is the standard deviation of the distribution of $\mathcal{P}_{\text{macro}}$).
- **BAM1** (Ballistic Aggregation with one Migration): Spherical monomers arrive on random trajectories. For $N > 2$: after first contact, the new arrival rolls to the nearest point where it can be in contact with a second sphere, and “sticks” there. For $N = 256$, BAM1 aggregates have $\mathcal{P}_{\text{macro}} \approx 0.739 \pm 0.018$ (Shen et al. 2008).

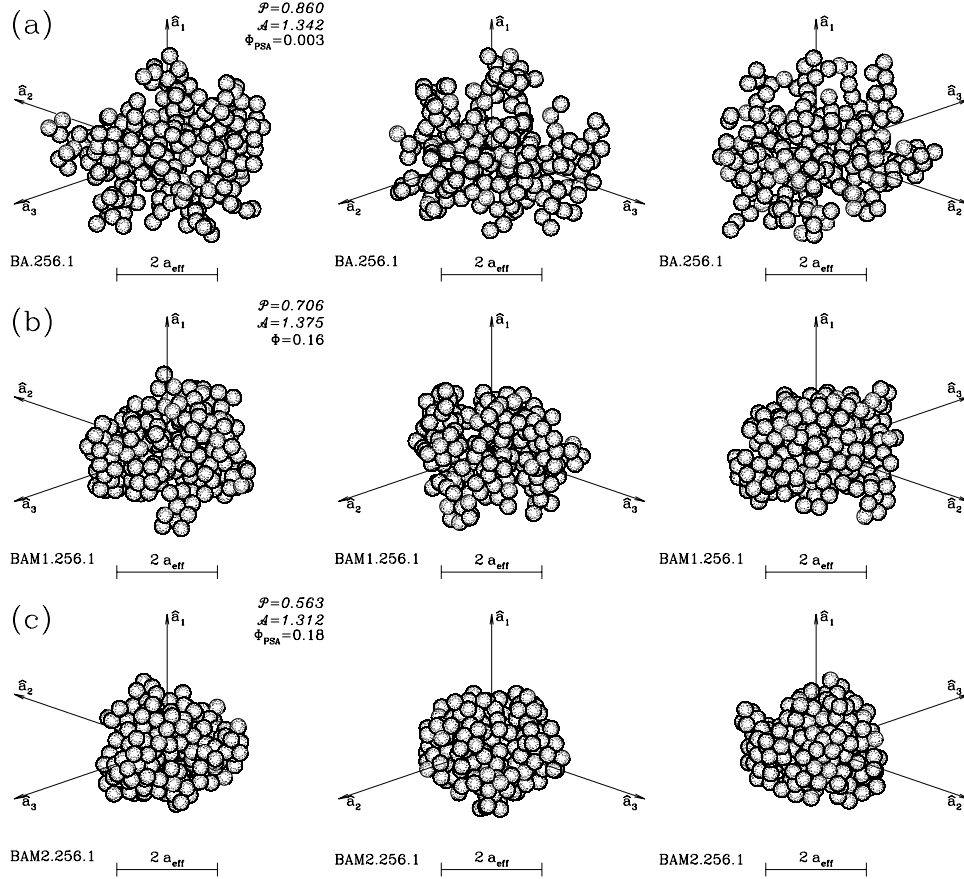


Figure 3. Random aggregates (a) BA.256.1, (b) BAM1.256.1, and (c) BAM2.256.1, each from 3 viewing angles.⁵ $\hat{\mathbf{a}}_1$ is the principal axis of largest moment of inertia; grains are assumed to spin around this axis. Macroporosity $\mathcal{P}_{\text{macro}}$ and asymmetry factor \mathcal{A} are given. Scale bars show $2a_{\text{eff}}$, the diameter of an equal-solid-volume sphere.

- **BAM2** (Ballistic Aggregation with two Migrations): Spherical “monomers” arrive on random trajectories. For $N > 2$: after first contact, the new arrival rolls to the nearest point where it can be in contact with two other spheres. If $N > 3$, it then rolls to the nearest point where it can make contact with a third sphere, and “sticks” there. For $N = 256$, BAM2 aggregates have $\mathcal{P}_{\text{macro}} \approx 0.579 \pm 0.026$ (Shen et al. 2008).

Figure 3 shows one random realization of each of these aggregate types.⁵

3.3. $N = 256$ Trimmed Aggregates

In addition to the BA, BAM1, and BAM2 random aggregates described above, we also study aggregates that have been trimmed to make them more flattened or elongated. We first construct random aggregates following the BA, BAM1 and BAM2 prescriptions, and find the principal axes $\hat{\mathbf{a}}_1$, $\hat{\mathbf{a}}_2$, $\hat{\mathbf{a}}_3$. We then systematically remove spheres in a manner designed to make the final structure either more flattened or more elongated. Let \mathbf{r}_j be the center of sphere j , with the initial centroid at $\mathbf{r} = 0$.

⁵ See http://www.astro.princeton.edu/~draine/Draine.2024b_suppmat.html for additional examples of each of these random aggregate types, as well as extinction and polarization cross sections for every example in Table 1.

Table 1. Geometric Parameters for the Considered Shapes

N	shape	axial ratios	α_1	α_2	α_3	\mathcal{A}^a	\mathcal{S}^b	$\mathcal{P}_{\text{macro}}^c$
2	bisphere	1 : 1 : 2	2.2049	2.2049	0.6300	1.871	1.871	0.184
3	threesphere	1 : 1 : 3	3.6857	3.6857	0.4808	2.769	2.769	0.208
3	trisphere	1 : 1.87 : 2	2.0833	1.2820	1.2820	2.082	0.785	0.308
256	BA.256.1	1 : 1.10 : 1.22	4.5421	3.8713	3.1928	1.342	1.017	0.860
256	BA.256.2	1 : 1.20 : 1.40	4.5146	3.9351	2.9464	1.381	1.079	0.852
256	BA.256.3	1 : 1.18 : 1.28	4.5474	3.7800	3.1125	1.387	1.010	0.855
256	BA.256.4	1 : 1.10 : 1.37	3.8261	3.5056	3.1018	1.173	1.018	0.842
256	BAM1.256.1	1 : 1.09 : 1.43	2.8462	2.5011	1.8513	1.375	1.090	0.706
256	BAM1.256.2	1 : 1.21 : 1.42	3.2580	2.7559	1.9919	1.479	1.082	0.741
256	BAM1.256.3	1 : 1.04 : 1.60	2.7464	2.6270	1.7413	1.301	1.201	0.698
256	BAM1.256.4	1 : 1.05 : 1.32	3.0355	2.7150	2.1538	1.287	1.062	0.752
256	BAM2.256.1	1 : 1.28 : 1.30	2.0827	1.6846	1.6078	1.312	0.921	0.563
256	BAM2.256.2	1 : 1.18 : 1.43	2.3293	1.9550	1.4589	1.466	1.061	0.578
256	BAM2.256.3	1 : 1.00 : 1.37	2.2886	2.1853	1.3588	1.350	1.239	0.582
256	BAM2.256.4	1 : 1.27 : 1.31	2.2880	1.9949	1.6011	1.323	1.042	0.612
256	BAttrimA.256.1	1 : 1.10 : 2.09	5.5978	5.2975	2.0947	1.766	1.547	0.837
256	BAttrimA.256.2	1 : 1.00 : 2.15	5.9604	5.6640	1.9524	1.897	1.660	0.833
256	BAttrimA.256.3	1 : 1.19 : 2.61	6.5335	6.0392	1.8181	2.222	1.752	0.826
256	BAttrimA.256.4	1 : 1.23 : 2.15	5.0958	4.9174	1.8739	1.734	1.591	0.812
256	BAM1trimA.256.1	1 : 1.15 : 2.57	4.0083	3.7684	1.2284	2.014	1.698	0.676
256	BAM1trimA.256.2	1 : 1.13 : 2.38	4.3939	4.1387	1.2761	2.075	1.748	0.703
256	BAM1trimA.256.3	1 : 1.10 : 2.40	3.9182	3.7365	1.2240	1.939	1.706	0.674
256	BAM1trimA.256.4	1 : 1.31 : 2.23	4.1224	3.5831	1.4893	2.083	1.446	0.711
256	BAM2trimA.256.1	1 : 1.08 : 2.15	2.7909	2.6722	1.1466	1.648	1.494	0.578
256	BAM2trimA.256.2	1 : 1.27 : 2.65	3.4278	3.2202	0.9193	2.195	1.814	0.533
256	BAM2trimA.256.3	1 : 1.06 : 2.23	3.6061	3.5617	0.8524	2.113	2.032	0.533
256	BAM2trimA.256.4	1 : 1.11 : 2.31	3.0484	2.8989	1.0067	1.886	1.655	0.548
256	BAttrimB.256.1	1 : 3.06 : 3.29	6.9806	4.4450	3.3357	2.954	0.921	0.838
256	BAttrimB.256.2	1 : 3.09 : 3.52	7.6158	4.7914	3.4839	3.398	0.930	0.836
203	BAttrimB.256.3	1 : 2.50 : 2.70	6.5451	4.3900	3.0701	2.675	0.979	0.837
256	BAttrimB.256.4	1 : 2.82 : 3.47	7.2562	4.6455	3.2323	3.417	0.959	0.822
256	BAM1trimB.256.1	1 : 2.67 : 3.40	4.6552	3.3062	1.9012	2.904	1.111	0.697
256	BAM1trimB.256.2	1 : 2.62 : 3.52	5.4627	3.7929	2.1502	3.372	1.107	0.723
256	BAM1trimB.256.3	1 : 2.81 : 3.69	4.9165	3.4406	1.9504	3.219	1.111	0.690
256	BAM1trimB.256.4	1 : 2.95 : 3.39	5.4628	3.6533	2.2820	3.401	1.035	0.725
256	BAM2trimB.256.1	1 : 2.82 : 2.87	3.7554	2.1944	1.9714	3.025	0.807	0.584
256	BAM2trimB.256.2	1 : 3.42 : 3.66	4.1837	2.6593	1.8385	3.709	0.955	0.558
256	BAM2trimB.256.3	1 : 2.66 : 3.57	4.5707	3.4745	1.4238	3.735	1.362	0.577
256	BAM2trimB.256.4	1 : 2.73 : 3.18	3.9970	2.6027	1.7863	3.197	0.974	0.591
256	BAttrimC.256.1	1 : 4.05 : 4.99	9.0308	5.4698	4.0287	4.830	1.109	0.838
256	BAttrimC.256.2	1 : 4.13 : 5.10	7.4399	4.6722	3.3762	3.497	0.932	0.825
256	BAM1trimC.256.1	1 : 3.68 : 5.34	7.2802	5.3448	2.2033	5.212	1.335	0.706
256	BAM1trimC.256.2	1 : 4.08 : 6.49	9.0775	6.9573	2.3396	6.432	1.510	0.727
256	BAM2trimC.256.1	1 : 5.51 : 5.53	6.4871	3.4908	3.1687	6.135	0.770	0.628
256	BAM2trimC.256.2	1 : 5.72 : 7.08	6.9519	4.2215	2.6719	6.994	1.026	0.606

^a Asymmetry parameter (Eq. 3).^b Stretch parameter (Eq. 3 in [Draine 2024](#)).^c Macroporosity parameter (Eq. 4).

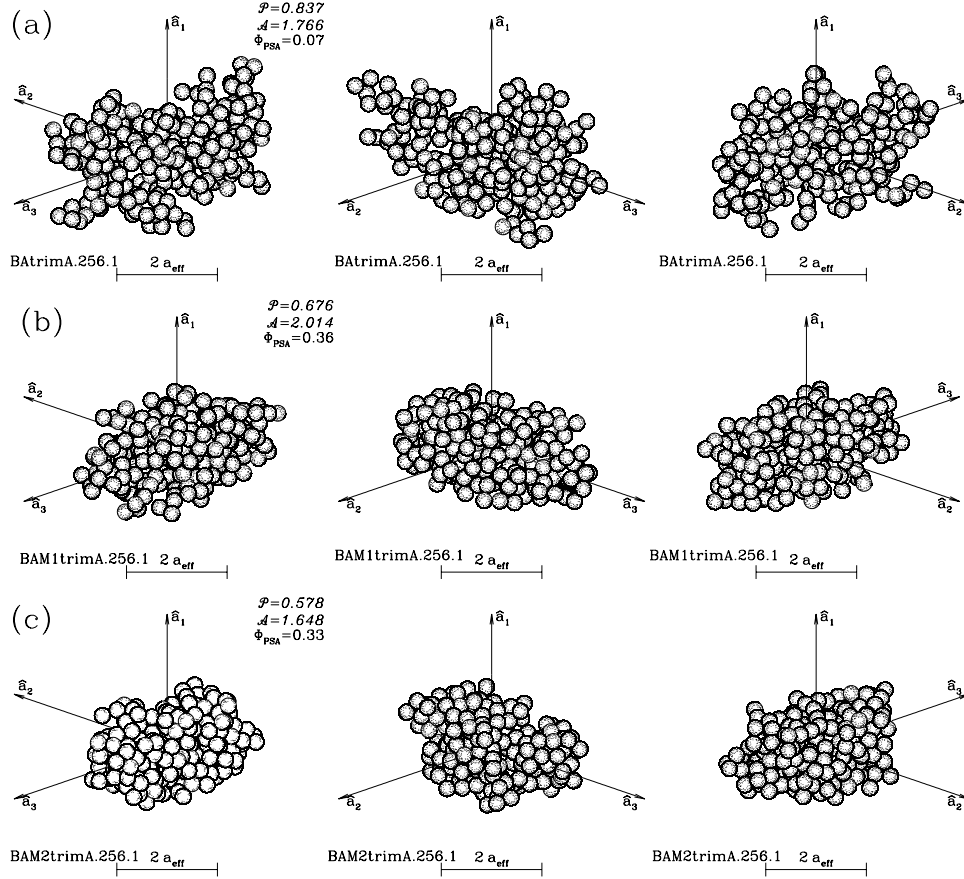


Figure 4. Same as Figure 3, but for BA, BAM1, and BAM2 clusters modified by the *trimA* procedure.⁵

We consider three types of trimmed aggregates of M spheres:

- ***trimA***: Start with a $N = 2M$ random aggregate (BA or BAM1 or BAM2). Remove the sphere with the largest value of $\mathbf{r}_j \cdot \hat{\mathbf{a}}_1$, next remove the sphere with the most negative value of $\mathbf{r}_j \cdot \hat{\mathbf{a}}_1$, next remove the sphere with the largest value of $\mathbf{r}_j \cdot \hat{\mathbf{a}}_2$, then remove the sphere with the most negative value of $\mathbf{r}_j \cdot \hat{\mathbf{a}}_2$. Repeat and continue until M spheres remain. This process tends to produce elongated structures, extended in the $\hat{\mathbf{a}}_3$ direction – see Figure 4.
- ***trimB***: Start with a $N = 2M$ random aggregate (BA or BAM1 or BAM2). Remove the sphere with the largest value of $\mathbf{r}_j \cdot \hat{\mathbf{a}}_1$, then remove the sphere with the most negative value of $\mathbf{r}_j \cdot \hat{\mathbf{a}}_1$. Repeat and continue until M spheres remain. This process tends to produce flattened structures, extended in the $\hat{\mathbf{a}}_2 - \hat{\mathbf{a}}_3$ plane – see Figure 5.
- ***trimC***: Same as *trimB*, but starting with a $N = 4M$ random aggregate. Because 75% of the original spheres have been removed, the *trimC* aggregates tend to be more flattened than the *trimB* aggregates – see Figure 6.

For each of these procedures: after each removal, check to see if any of the remaining spheres or groups of spheres have become disconnected from the main body; if so, remove them. This procedure can sometimes result in a trimmed aggregate with fewer than the intended final number of M spheres, although this occurred for only one⁶ of the examples encountered in the present study.⁷

⁶ Target BAttrimB.256.3 consists of $N = 203$ spheres.

⁷ The *trimA*, *trimB*, and *trimC* aggregates studied here can be found at www.astro.princeton.edu/~draine/agglom.html.

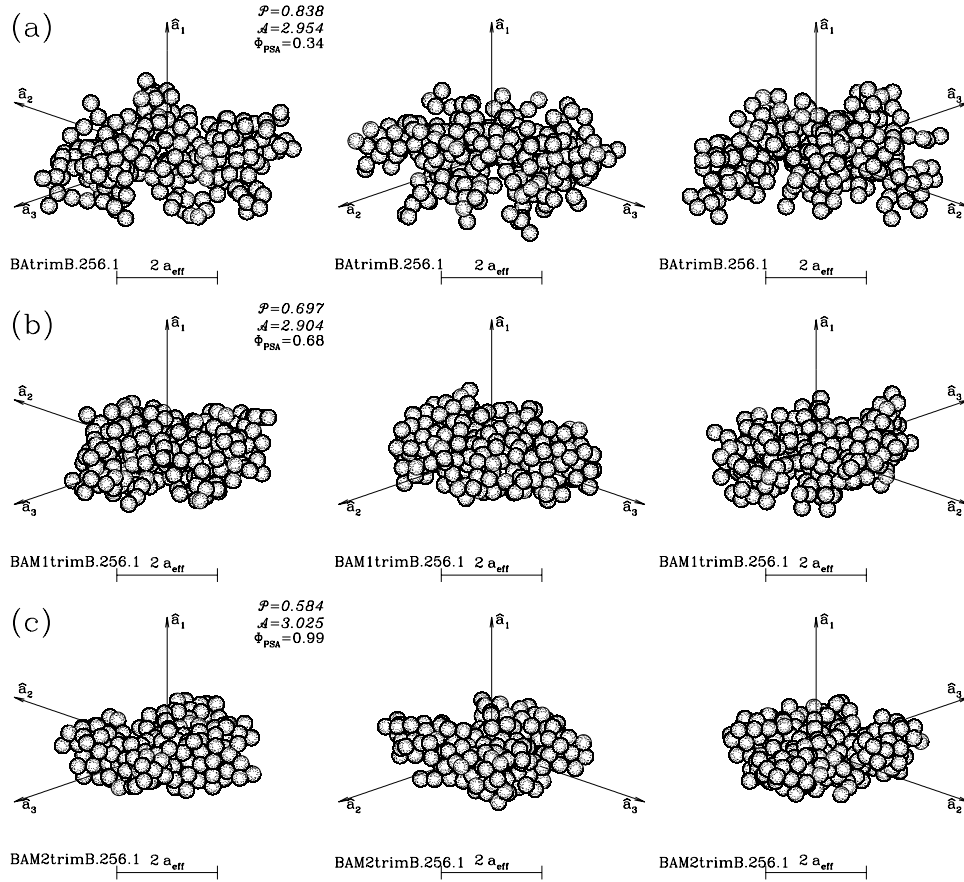


Figure 5. Same as Figure 3, but for aggregates created by the *trimB* procedure: (a) BAtrimB.256.1, (b) BAM1trimA.256.1, and (c) BAM2trimB.256.1.⁵

For each aggregate we find the α_j , $\mathcal{P}_{\text{macro}}$, and \mathcal{A} : see Table 1. We also measure the spatial extent of the aggregate along the $\hat{\mathbf{a}}_1$, $\hat{\mathbf{a}}_2$, $\hat{\mathbf{a}}_3$ directions, resulting in the “axial ratios” listed in Table 1.

The BAM2trimB and BAM2trimC aggregates are the most asymmetric shapes considered here (see Figures 5 and 6), but their asymmetries do not seem especially extreme when compared to the IDPs in Figure 1.

4. SCATTERING AND ABSORPTION

4.1. Discrete Dipole Approximation

Cross sections for scattering and absorption are calculated using the DDA, for wavelengths λ from the FUV ($\lambda = 0.1\mu\text{m}$) to the FIR ($\lambda = 100\mu\text{m}$). We use the public-domain code DDSCAT⁸ (Draine & Flatau 1994). For the solid material we use the Astro dust dielectric function obtained by Draine & Hensley (2021b) for 5:7:7 oblate spheroids with $\mathcal{P}_{\text{micro}} = 0.2$ (the “oblate” dielectric function in Figure 2 of Paper I). Our goal is to explore the effects of shape for a fixed dielectric function for the solid material.

Calculations are carried out for 151 wavelengths from $0.1\mu\text{m}$ to $100\mu\text{m}$, uniformly spaced in $\log \lambda$. For each shape, we consider 6 values of a_{eff} between $0.05\mu\text{m}$ to $0.30\mu\text{m}$; for some shapes we extend the calculations to larger values of a_{eff} as required to have the linear polarization peaking near $\lambda = 0.55\mu\text{m}$

⁸ DDSCAT 7.3.3, available at www.ddscat.org

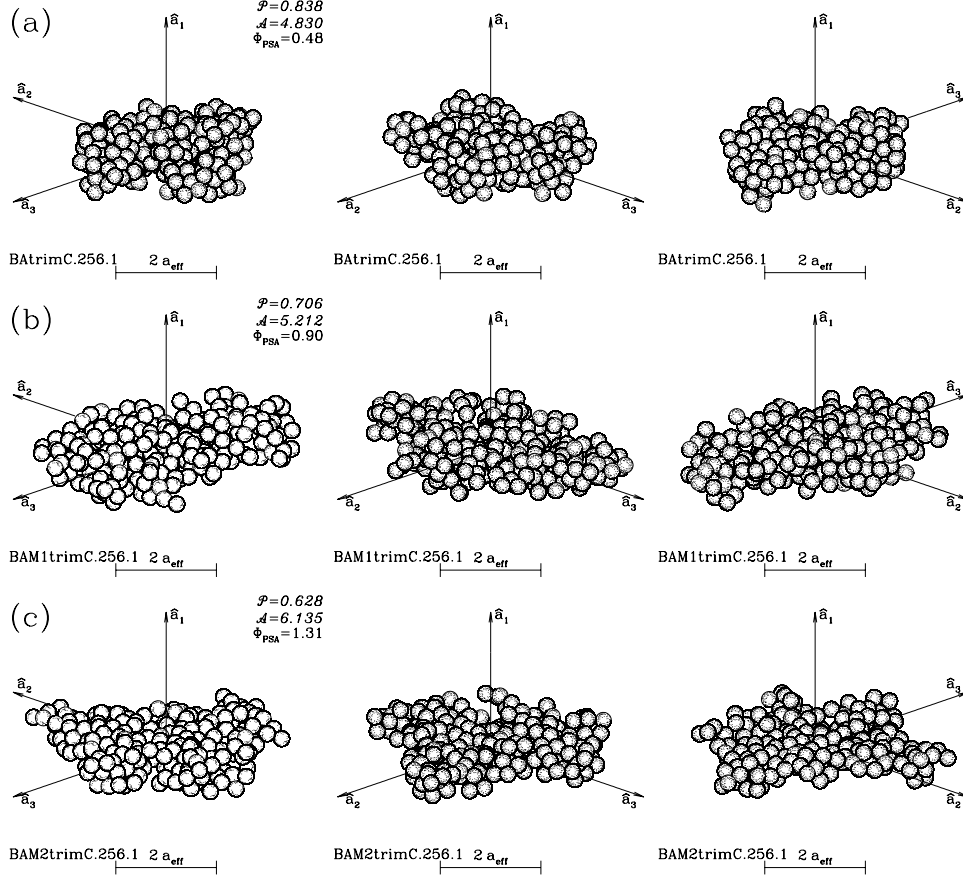


Figure 6. Same as Figure 3, but for aggregates created by the *trimC* procedure: (a) BAtrimC.256.1, (b) BAM1trimC.256.1, and (c) BAM2trimC.256.1.⁵

as in the interstellar medium. As in Paper I, for each shape, size a_{eff} , orientation, and wavelength λ , we calculate cross sections for two orthogonal linear polarizations using three different numbers N_d of dipoles, and then extrapolate cross sections to $N_d \rightarrow \infty$ using Equation (8) of Paper I. See Appendix A for further details.

4.2. Orientational Averages

4.2.1. Extinction

For each shape and size a_{eff} , and wavelength λ , we calculate the extinction cross section, $C_{\text{ext}} \equiv C_{\text{abs}} + C_{\text{sca}}$, averaged over random orientations:

$$C_{\text{ext,ran}}(\lambda) \equiv \langle C_{\text{ext}}(\lambda) \rangle_{\text{ran}} . \quad (6)$$

Orientational averaging is discussed in Appendix D of Paper I. In brief, let Θ be the angle between the direction of propagation $\hat{\mathbf{k}}$ and an axis $\hat{\mathbf{a}}$ fixed in the grain. Let β be an angle for rotation of the grain around axis $\hat{\mathbf{a}}$. For extinction, we average over both incident polarization states.

For the bisphere and threesphere we let $\hat{\mathbf{a}}$ be the axis of rotational symmetry. These shapes have reflection symmetry (β is irrelevant). We sample uniformly in $\cos \Theta \in [0, 1]$ (11 values of $\cos \Theta$).

For the trisphere we take $\hat{\mathbf{a}} = \hat{\mathbf{a}}_1$, the axis of 3-fold rotational symmetry. The trisphere also has reflection symmetry. We sample uniformly in $\cos \Theta \in [0, 1]$ (11 values of $\cos \Theta$) and $\beta \in (0, \pi/3)$ (3 values of β), for a total of 33 orientations.

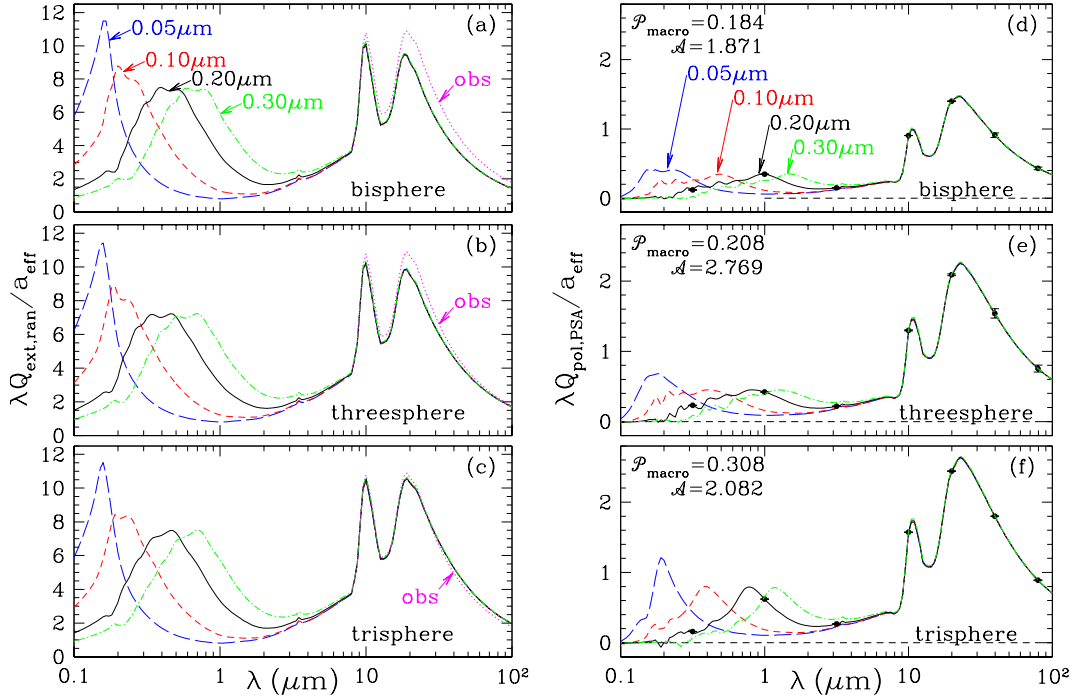


Figure 7. *a-c*: $\lambda Q_{\text{ext,ran}}/a_{\text{eff}}$ for bisphere, threesphere, and trisphere geometries (see Figure 2) for $a_{\text{eff}} = 0.05, 0.1, 0.2, 0.3 \mu\text{m}$. For $\lambda > 8 \mu\text{m}$, the dotted curves show the “observed” value of $\lambda Q_{\text{abs}}/a_{\text{eff}}$ (see text). *d-f*: $\lambda Q_{\text{pol,PSA}}/a_{\text{eff}}$ for the same geometries. For $a_{\text{eff}} = 0.2 \mu\text{m}$, uncertainty intervals are shown at selected λ .

The $N = 256$ random aggregates have no symmetries. Letting $\hat{\mathbf{a}} = \hat{\mathbf{a}}_1$, we sample uniformly in $\cos \Theta \in [-1, 1]$ (11 values of Θ), and uniformly in $\beta \in (0, 2\pi)$ (12 values of β), for a total of 132 orientations.

4.2.2. Polarization

“Perfect spinning alignment” (PSA) is the optimal configuration for spinning grains to produce polarization: the grain is assumed to be spinning around $\hat{\mathbf{a}}_1$, the principal axis of largest moment of inertia, with $\hat{\mathbf{a}}_1$ parallel to the local magnetic field \mathbf{B}_0 , and radiation propagating perpendicular to $\hat{\mathbf{a}}_1$. For linear polarization states $\mathbf{E} \parallel \hat{\mathbf{a}}_1$, $\mathbf{E} \perp \hat{\mathbf{a}}_1$,

$$C_{\text{pol,PSA}}(\lambda) \equiv \frac{1}{2} \left\langle C_{\text{ext}}(\lambda, \mathbf{E} \perp \hat{\mathbf{a}}_1) - C_{\text{ext}}(\lambda, \mathbf{E} \parallel \hat{\mathbf{a}}_1) \right\rangle_{\text{PSA}} . \quad (7)$$

For the bisphere and threesphere ($\hat{\mathbf{a}}_1 \perp \hat{\mathbf{a}}$) we interpolate among the 11 values of $\cos \Theta \in [0, 1]$ to average over Θ .

For the trisphere ($\hat{\mathbf{a}}_1 = \hat{\mathbf{a}}$), we set $\Theta = \pi/2$ and average over β (3 values $\in [0, \pi/3]$).

For the random aggregates ($\hat{\mathbf{a}}_1 = \hat{\mathbf{a}}$), we set $\Theta = \pi/2$, and average over rotations around $\hat{\mathbf{a}}_1$ (12 values of $\beta \in (0, 2\pi)$).

5. RESULTS: EXTINCTION AND POLARIZATION BY AGGREGATES

5.1. Extinction

We define the usual dimensionless efficiency factors:

$$Q_x(\text{shape}, \lambda) \equiv \frac{C_x(\text{shape}, \lambda)}{\pi a_{\text{eff}}^2} , \quad (8)$$

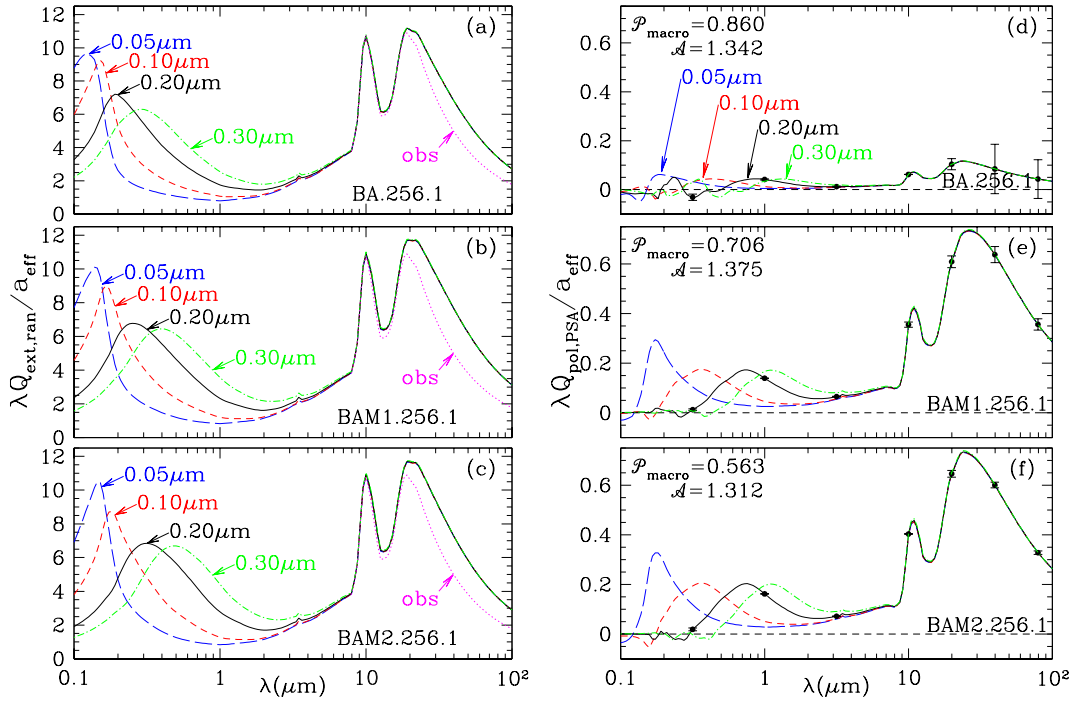


Figure 8. Same as Figure 7, but for examples of $N = 256$ BA, BAM1, and BAM2 aggregates (see Figure 3).⁵ Panels *d, e, f*: Note change of scale relative to Figure 7 – these random aggregates are ineffective polarizers.

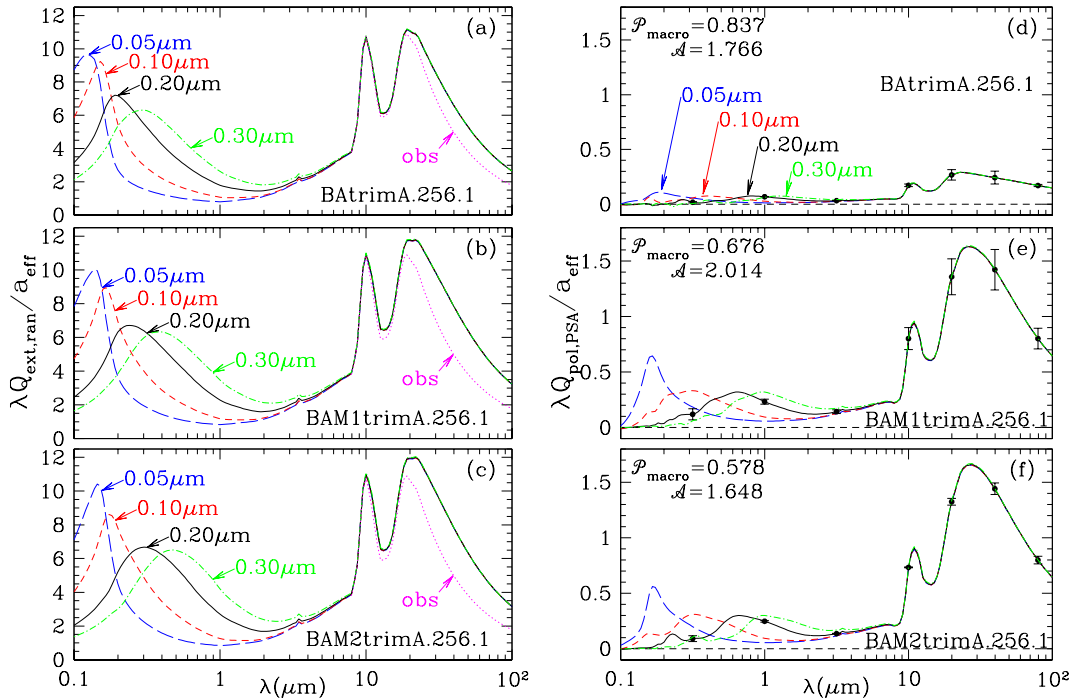


Figure 9. Same as Figure 7, but for “*trimA*” aggregates (see Figure 4).⁵ Panels *d, e, f*: Note change of scale relative to Figure 8.

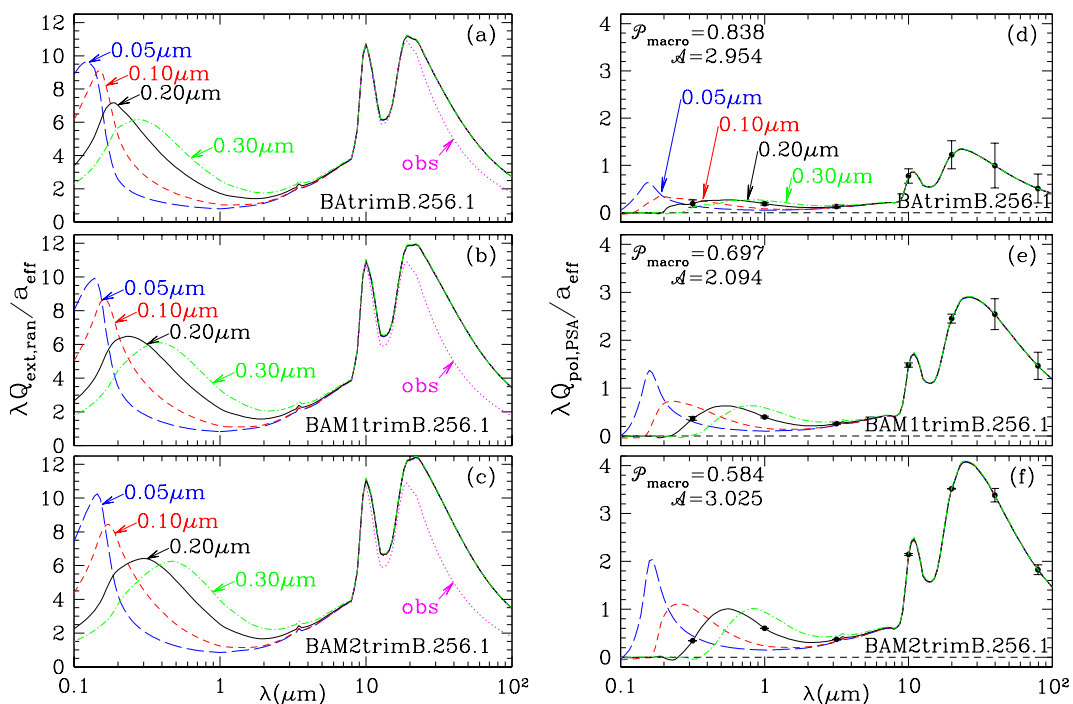


Figure 10. Same as Figure 7, but for “*trimB*” aggregates (see Figure 5).⁵ Panels *d,e,f*: Note change of scale relative to Figure 8.

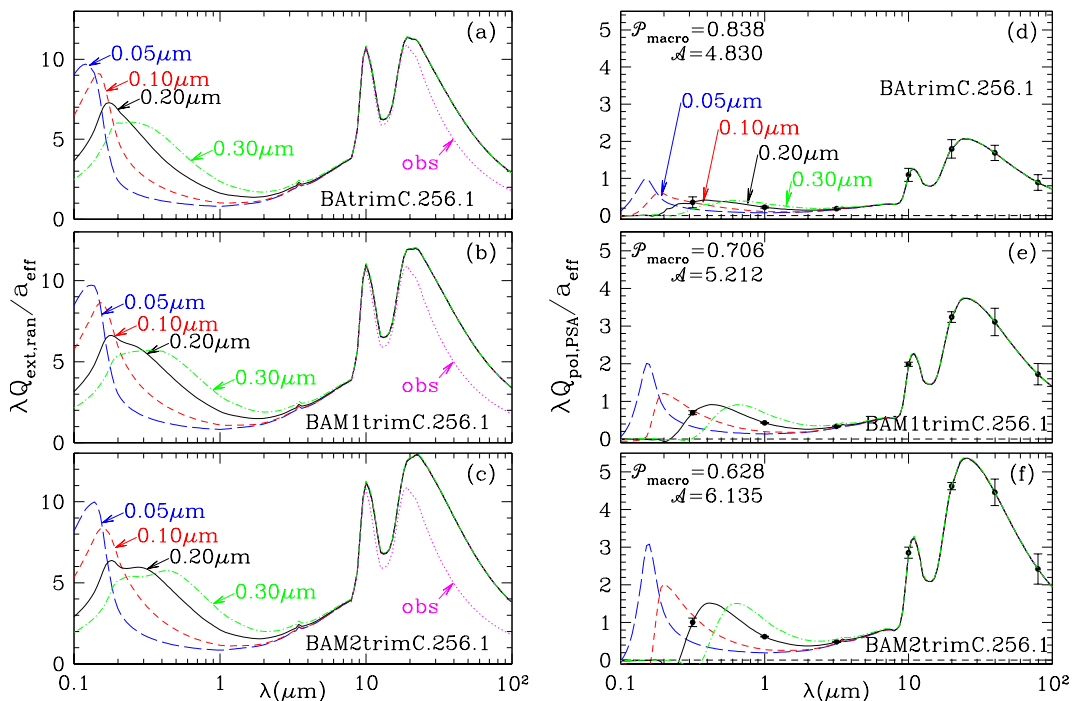


Figure 11. Same as Figure 7, but for “*trimC*” aggregates (see Figure 6).⁵ Panels *d,e,f*: Note change of scale relative to Figure 8.

where C_x is a cross section. Cross sections per unit solid volume are proportional to Q_x/a_{eff} :

$$\frac{C_x(\text{shape}, \lambda)}{V_{\text{solid}}} = \frac{3}{4} \frac{Q_x(\text{shape}, \lambda)}{a_{\text{eff}}} . \quad (9)$$

Figures 7–11 show the dimensionless quantities $\lambda Q_{\text{ext,ran}}/a_{\text{eff}}$ for extinction by randomly-oriented particles, and $\lambda Q_{\text{pol,PSA}}/a_{\text{eff}}$ for particles in “perfect spinning alignment” (PSA), for one example of each of the shape classes studied here, from the FUV ($\lambda = 0.1\mu\text{m}$) to the FIR ($\lambda = 100\mu\text{m}$). For each shape, results are shown for four sizes a_{eff} .

The extinction cross sections per unit volume have broadly similar behavior. For $a_{\text{eff}} \approx 0.2\mu\text{m}$ and $\lambda \lesssim 1\mu\text{m}$, where scattering is important, $\lambda Q_{\text{ext,ran}}/a_{\text{eff}}$ has a broad peak, with peak value $\lambda Q_{\text{ext,ran}}/a_{\text{eff}} \approx 7$ near

$$\lambda_{\text{max},\lambda Q_{\text{ext}}} \approx 2.5 (1 - \mathcal{P}_{\text{macro}})^{1/3} a_{\text{eff}} , \quad (10)$$

e.g., for $a_{\text{eff}} = 0.2\mu\text{m}$, $\lambda_{\text{max},\lambda Q_{\text{ext}}} \approx 0.4\mu\text{m}$ for the bisphere ($\mathcal{P}_{\text{macro}} = 0.18$, Figure 7a), and $0.2\mu\text{m}$ for BA.256.1 ($\mathcal{P}_{\text{macro}} \approx 0.85$, Figure ??a).

For $\lambda \gtrsim 5\mu\text{m}$, the grains have $a_{\text{eff}} \ll \lambda$, scattering is small compared to absorption ($C_{\text{ext}} \approx C_{\text{abs}}$), and $\lambda Q_{\text{ext}}/a_{\text{eff}} = (4/3)\lambda C_{\text{ext}}/V_{\text{solid}}$ depends only on the shape and dielectric function (and therefore λ), but not on a_{eff} . For the “astrodust” dielectric function, with strong absorption in the silicate features near $10\mu\text{m}$ and $18\mu\text{m}$, all shapes have $\lambda Q_{\text{ext,ran}}/a_{\text{eff}}$ peaking at $\sim 10\mu\text{m}$ and $\sim 20\mu\text{m}$, with peak values ranging from ~ 10 for the $N = 2$ and $N = 3$ aggregates (Figure 7), to ~ 12 for the $N = 256$ aggregates (Figures 8-11).

Figures 7-11 also show the observed value of $\lambda Q_{\text{abs}}/a_{\text{eff}} = (4\lambda/3)C_{\text{abs}}/V_{\text{solid}}$ for $\lambda > 8\mu\text{m}$ (Hensley & Draine 2021).

For a fixed dielectric function, the opacity depends on the grain shape. The dielectric function used in all calculations in the present paper was devised so that randomly-oriented 1.4:1 oblate spheroids would reproduce the observed IR-submm opacity (Draine & Hensley 2021a). Figure 7 shows that the trisphere geometry provides nearly the same opacity as the 1.4:1 oblate spheroid (i.e., the curve labelled “obs”); the bisphere provides somewhat *less* absorption.

The present study uses the same dielectric function for all shapes. The high porosity of the BA, BAM1, and BAM2 aggregates results in enhanced absorption: at $\lambda = 100\mu\text{m}$, the BA, BAM1, BAM2 examples provide more opacity than the 1.4:1 oblate spheroid, by factors ranging from 1.8–2.3 (see Figure 8). A fully self-consistent approach would require that for each shape we derive a new dielectric function that would reproduce the observed absorption at long wavelengths. For spheroidal shapes, Draine & Hensley (2021a) developed an iterative technique employing the analytic result for absorption by spheroids in the Rayleigh limit. Unfortunately, analytic results for these complex shapes are unavailable. The numerically difficult problem of devising a self-consistent dielectric function for these complex shapes is deferred to future work.

5.2. Polarization

The polarization cross sections vary greatly from one aggregate to another. The original BA, BAM1, and BAM2 aggregates (see Figure 8) are ineffective polarizers. The polarization cross section per volume varies considerably from one random realization to another, but with a general trend of decreasing $Q_{\text{pol,PSA}}/a_{\text{eff}}$ as the porosity increases from $\mathcal{P}_{\text{macro}} \approx 0.58$ to $\mathcal{P}_{\text{macro}} \approx 0.85$.

Of the 45 nonconvex shapes studied here, the BAM2trimB and BAM2trimC geometries, with $\mathcal{P}_{\text{macro}} \approx 0.58$ and aspect ratios in the range 2.8-7 (see Table 1) have the highest polarization cross section per volume, both in the optical and in the infrared (see Figure 10c): for the BAM2trimC.256.1 aggregate with $a_{\text{eff}} = 0.20\mu\text{m}$, $\lambda Q_{\text{pol,PSA}}/a_{\text{eff}}$ peaks at ~ 6 in the optical, and ~ 5 near $25\mu\text{m}$. The strength of the polarization will be discussed further in Section 7 below.

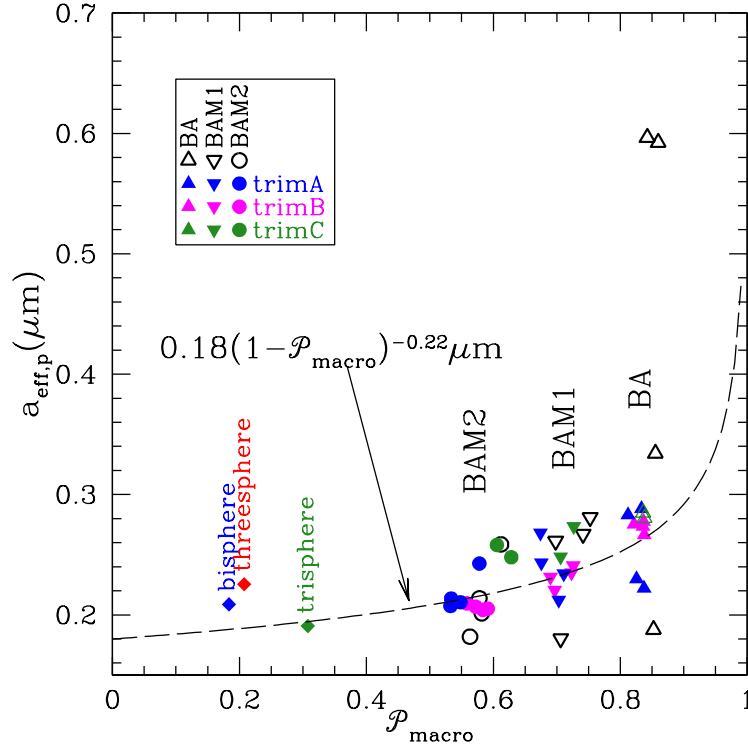


Figure 12. Effective radius $a_{\text{eff,p}}$ such that aggregate has $\lambda_p = 0.567\mu\text{m}$, plotted against macroporosity $\mathcal{P}_{\text{macro}}$. Broken line: Eq. (12).

6. STARLIGHT POLARIZATION: EFFECTIVE WAVELENGTH λ_p AND PROFILE WIDTH σ_p

Draine & Hensley (2021a) showed that interstellar grains must have certain integral properties to be compatible with the observed polarization of starlight. For a grain with a given shape and size a_{eff} , the effective wavelength for polarization of starlight is defined to be

$$\lambda_p(\text{shape}, a_{\text{eff}}) \equiv \exp \left[\frac{\int_{\lambda_1}^{\lambda_2} \ln \lambda Q_{\text{pol,PSA}}(\lambda) d \ln \lambda}{\int_{\lambda_1}^{\lambda_2} Q_{\text{pol,PSA}}(\lambda) d \ln \lambda} \right], \quad (11)$$

with $\lambda_1 = 0.15\mu\text{m}$ and $\lambda_2 = 2.5\mu\text{m}$ to cover the wavelength range over which starlight polarization is well-observed.

To be consistent with the average observed polarization of starlight (peaking at $\lambda_{\text{max}} \approx 0.55\mu\text{m}$), dust grains should have sizes a_{eff} near a characteristic size $a_{\text{eff,p}}$ for which $\lambda_p \approx 0.567\mu\text{m}$ (see Paper I). Using $\lambda_p(\text{shape}, a_{\text{eff}})$ calculated for selected sizes a_{eff} , we interpolate to estimate $a_{\text{eff,p}}(\text{shape})$; the results are shown in Figure 12 and Table 2. The aligned grains responsible for starlight polarization have a distribution of sizes, but the distribution should be peaked near $a_{\text{eff,p}}$ in order for the starlight polarization to peak near $\lambda_{\text{max}} \approx 0.55\mu\text{m}$.

The convex shapes in Paper I (Draine 2024) had $a_{\text{eff,p}} \approx 0.18\mu\text{m}$. For the 45 non-convex shapes in the present study, Figure 12 shows that $a_{\text{eff,p}}$ tends to increase with increasing $\mathcal{P}_{\text{macro}}$. With the exception of the BA aggregates (which are very poor polarizers), the other shapes are approximately consistent with the empirical relation

$$a_{\text{eff,p}} \approx 0.18\mu\text{m}(1 - \mathcal{P}_{\text{macro}})^{-0.22}, \quad (12)$$

although individual shapes in Figure 12 scatter above or below Equation (12) by $\pm 15\%$ or so. The characteristic mass of the polarizing grains is

$$M_p = \frac{4\pi}{3} \rho_{\text{solid}} a_{\text{eff,p}}^3 \approx 7 \times 10^{-14} (1 - \mathcal{P}_{\text{macro}})^{-0.66} \text{ g} \quad , \quad (13)$$

where we have assumed $\rho_{\text{solid}} \approx 2.74 \text{ g cm}^{-3}$ for astrodust material with $\mathcal{P}_{\text{micro}} \approx 0.2$ (Draine & Hensley 2021c). The characteristic linear extent of the polarizing grains is

$$D_p \approx (1 - \mathcal{P}_{\text{macro}})^{-1/3} \times (2a_{\text{eff,p}}) \approx 0.36(1 - \mathcal{P}_{\text{macro}})^{-0.55} \mu\text{m} \quad , \quad (14)$$

In the ISM, the observed dependence of starlight polarization $p_{\text{obs}}(\lambda)$ on wavelength arises from a mixture of grain sizes. To reproduce the observed wavelength dependence $p_{\text{obs}}(\lambda)$, individual grains must have polarization profiles that are *narrower* than $p_{\text{obs}}(\lambda)$. The width of the polarization profile for a single grain size and shape is measured by the dimensionless quantity

$$\sigma_p(\text{shape}, a_{\text{eff}}) \equiv \left[\frac{\int_{\lambda_1}^{\lambda_2} [\ln(\lambda/\lambda_p)]^2 |Q_{\text{pol,PSA}}(\text{shape}, a_{\text{eff}}, \lambda)| d \ln \lambda}{\int_{\lambda_1}^{\lambda_2} |Q_{\text{pol,PSA}}(\text{shape}, a_{\text{eff}}, \lambda)| d \ln \lambda} \right]^{1/2} \quad . \quad (15)$$

(Draine & Hensley 2021a). In Paper I, it was argued that individual grains should have $\sigma_p < 0.6$ in order to be able to reproduce the observed polarization profile. Table 2 lists $\sigma_p(\text{shape}, a_{\text{eff,p}})$ for each shape.

7. STARLIGHT POLARIZATION EFFICIENCY INTEGRAL

If a candidate grain shape is to account for the strength of the observed starlight polarization, it must be a relatively efficient polarizer. Draine & Hensley (2021a) defined the dimensionless starlight polarization efficiency integral for grains in perfect spinning alignment:

$$\Phi_{\text{PSA}}(a_{\text{eff}}, \text{shape}) \equiv \int_{\lambda_1}^{\lambda_2} \frac{C_{\text{pol,PSA}}(\text{shape}, a_{\text{eff}}, \lambda)}{V_{\text{solid}}} d\lambda \quad . \quad (16)$$

Based on estimates for the solid volume per H nucleon, and observations of starlight polarization per unit H column density, Draine & Hensley (2021a) showed that the grains responsible for the polarization must have $\Phi_{\text{PSA}} \gtrsim 0.7$. For the astrodust dielectric function for $\mathcal{P}_{\text{micro}} = 0.2$, the requirement $\Phi_{\text{PSA}} > 0.7$ was satisfied by oblate spheroids with axial ratio ≥ 1.4 , or prolate spheroids with axial ratio ≥ 2 (Draine & Hensley 2021a).

Table 2 gives $\Phi_{\text{PSA}}(a_{\text{eff,p}})$ for the 45 shapes studied here, and Figure 13 shows $\Phi_{\text{PSA}}(a_{\text{eff,p}})$ and $\sigma_p(a_{\text{eff,p}})$.

The original BA, BAM1, and BAM2 geometries, with asymmetry parameters $\mathcal{A} < 1.48$, are not sufficiently asymmetric to account for the observed polarization. Macroporosities $\mathcal{P}_{\text{macro}} > 0.5$ are only viable if the aggregate is more flattened or elongated than the results of the BA, BAM1, or BAM2 random aggregation processes. Ten of the “trimmed” BAM1 and BAM2 aggregates (with $\mathcal{P}_{\text{macro}}$ as large as 0.72) are sufficiently flattened or elongated to be able to satisfy the requirement $\Phi_{\text{PSA}} > 0.7$ (see Figure 13).

Using the DDA to obtain Φ_{PSA} for a given shape and size is computationally demanding. It would be valuable to be able to estimate $\Phi_{\text{PSA}}(a_{\text{eff,p}})$ from $\mathcal{P}_{\text{macro}}$ and a simple measure of grain geometric asymmetry. Figure 14 shows that the calculated values of $\Phi(\text{shape}, a_{\text{eff,p}})$ are approximately consistent with a simple empirical relation:

$$\Phi_{\text{PSA}}(\text{shape}, a_{\text{eff,p}}) \approx 1.2(\psi - 0.07) \quad (17)$$

$$\psi \equiv (\mathcal{A} - 1)^{0.6} (1 - \mathcal{P}_{\text{macro}})^{0.8} \quad (18)$$

Table 2. Polarization Parameters for Nonconvex Shapes^a

shape	$a_{\text{eff,p}}(\mu\text{m})^b$	$\Phi_{\text{PSA}}(a_{\text{eff,p}})^c$	$[p_{\text{em}}(\text{FIR})]_{\text{max}}^d$	$\sigma_{\text{p}}(a_{\text{eff,p}})^e$
bisphere	0.209	0.373 ± 0.001	0.176 ± 0.006	0.603 ± 0.001
threesphere	0.226	0.538 ± 0.001	0.265 ± 0.011	0.599 ± 0.003
trisphere	0.191	0.686 ± 0.002	0.274 ± 0.001	0.575 ± 0.001
BA.256.1	0.592	0.003 ± 0.002	0.008 ± 0.014	0.637 ± 0.067
BA.256.2	0.188	0.052 ± 0.007	0.005 ± 0.026	0.693 ± 0.016
BA.256.3	0.334	0.030 ± 0.001	-0.005 ± 0.047	0.781 ± 0.010
BA.256.4	0.600	0.006 ± 0.023	0.002 ± 0.014	0.465 ± 0.182
BAM1.256.1	0.180	0.162 ± 0.005	0.065 ± 0.005	0.549 ± 0.007
BAM1.256.2	0.267	0.232 ± 0.021	0.098 ± 0.007	0.585 ± 0.005
BAM1.256.3	0.261	0.095 ± 0.021	0.049 ± 0.020	0.694 ± 0.032
BAM1.256.4	0.281	0.131 ± 0.017	0.045 ± 0.006	0.597 ± 0.020
BAM2.256.1	0.182	0.182 ± 0.001	0.066 ± 0.002	0.534 ± 0.012
BAM2.256.2	0.214	0.356 ± 0.013	0.133 ± 0.004	0.560 ± 0.003
BAM2.256.3	0.201	0.191 ± 0.009	0.069 ± 0.015	0.593 ± 0.011
BAM2.256.4	0.259	0.154 ± 0.009	0.074 ± 0.005	0.640 ± 0.002
BAttrimA.256.1	0.222	0.074 ± 0.006	0.038 ± 0.008	0.682 ± 0.030
BAttrimA.256.2	0.288	0.144 ± 0.011	0.055 ± 0.013	0.643 ± 0.012
BAttrimA.256.3	0.230	0.139 ± 0.001	0.056 ± 0.008	0.615 ± 0.008
BAttrimA.256.4	0.283	0.125 ± 0.048	0.031 ± 0.010	0.711 ± 0.011
BAM1trimA.256.1	0.242	0.358 ± 0.048	0.146 ± 0.017	0.597 ± 0.065
BAM1trimA.256.2	0.212	0.298 ± 0.012	0.139 ± 0.010	0.542 ± 0.006
BAM1trimA.256.3	0.268	0.291 ± 0.085	0.136 ± 0.030	0.635 ± 0.025
BAM1trimA.256.4	0.233	0.415 ± 0.029	0.176 ± 0.011	0.529 ± 0.003
BAM2trimA.256.1	0.231	0.327 ± 0.003	0.149 ± 0.006	0.618 ± 0.003
BAM2trimA.256.2	0.214	0.579 ± 0.001	0.222 ± 0.010	0.548 ± 0.016
BAM2trimA.256.3	0.207	0.453 ± 0.011	0.191 ± 0.004	0.502 ± 0.072
BAM2trimA.256.4	0.211	0.350 ± 0.048	0.159 ± 0.018	0.634 ± 0.014
BAttrimB.256.1	0.267	0.337 ± 0.076	0.112 ± 0.048	0.545 ± 0.018
BAttrimB.256.2	0.274	0.447 ± 0.002	0.171 ± 0.013	0.527 ± 0.004
BAttrimB.256.3	0.278	0.285 ± 0.024	0.109 ± 0.008	0.569 ± 0.016
BAttrimB.256.4	0.270	0.434 ± 0.012	0.163 ± 0.012	0.520 ± 0.007
BAM1trimB.256.1	0.221	0.681 ± 0.034	0.262 ± 0.033	0.487 ± 0.008
BAM1trimB.256.2	0.235	0.756 ± 0.053	0.244 ± 0.017	0.492 ± 0.012
BAM1trimB.256.3	0.231	0.811 ± 0.020	0.241 ± 0.012	0.493 ± 0.004
BAM1trimB.256.4	0.241	0.744 ± 0.058	0.261 ± 0.001	0.508 ± 0.020
BAM2trimB.256.1	0.204	0.991 ± 0.005	0.225 ± 0.003	0.471 ± 0.001
BAM2trimB.256.2	0.210	1.220 ± 0.018	0.209 ± 0.004	0.467 ± 0.008
BAM2trimB.256.3	0.207	1.066 ± 0.024	0.224 ± 0.004	0.471 ± 0.003
BAM2trimB.256.4	0.205	0.960 ± 0.018	0.230 ± 0.001	0.474 ± 0.012
BAttrimC.256.1	0.285	0.484 ± 0.081	0.186 ± 0.016	0.501 ± 0.013
BAttrimC.256.2	0.281	0.527 ± 0.018	0.210 ± 0.004	0.499 ± 0.008
BAM1trimC.256.1	0.248	0.901 ± 0.036	0.244 ± 0.004	0.478 ± 0.002
BAM1trimC.256.2	0.273	0.905 ± 0.004	0.245 ± 0.007	0.488 ± 0.015
BAM2trimC.256.1	0.248	1.311 ± 0.054	0.206 ± 0.020	0.462 ± 0.002
BAM2trimC.256.2	0.258	1.475 ± 0.007	0.197 ± 0.004	0.469 ± 0.005

^a Cases with $\Phi_{\text{PSA}} > 0.7$ and $[p_{\text{em}}(\text{FIR})]_{\text{max}} \in [0.20, 0.26]$ are shown in bold.

^b a_{eff} such that $\lambda_{\text{p}} = 0.567 \mu\text{m}$ (see text).

^c Starlight polarization efficiency integral: Equation (16).

^d Maximum FIR-submm polarization fraction: Equation (8) from [Draine \(2024\)](#).

^e Polarization profile width parameter: Equation (15).

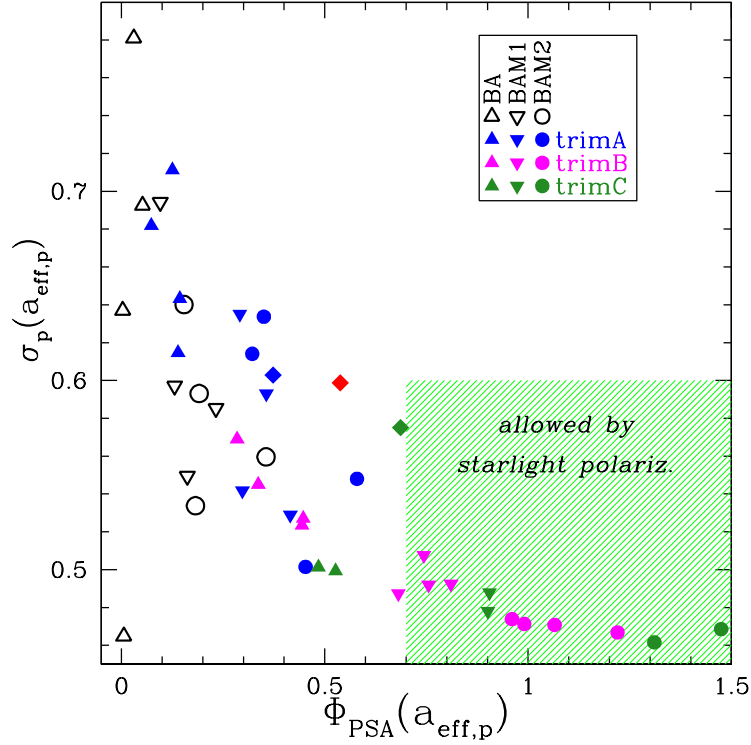


Figure 13. Polarization parameters σ_p and Φ_{PSA} for 45 aggregates, each with size $a_{\text{eff}} = a_{\text{eff,p}}$ such that $\lambda_p = 0.567\mu\text{m}$. The allowed region $\Phi_{\text{PSA}} > 0.7$, $\sigma_p < 0.6$ (see Paper I) is shown in green. Only the trisphere, BAM1trimB, BAM1trimC, BAM2trimB, and BAM2trimC geometries are within or close to the allowed region – other shapes considered here have Φ_{PSA} too small to account for the observed polarization of starlight.

for the 20 convex shapes (with $0 \leq \mathcal{P}_{\text{macro}} < 0.12$) in Paper I, and the 45 nonconvex aggregates (with $0.18 < \mathcal{P}_{\text{macro}} < 0.84$) studied here. Evidently the single parameter ψ is a good predictor of a given shape’s ability to polarize starlight. For shapes with $\Phi_{\text{PSA}}(a_{\text{eff,p}}) \gtrsim 0.3$, Eq. (17) predicts Φ_{PSA} to within $\sim \pm 20\%$, although there are a few conspicuous deviations [e.g., the bisphere and threesphere shapes fall a factor ~ 2 below Equation (17)].

The requirement $\Phi_{\text{PSA}}(a_{\text{eff,p}}) \gtrsim 0.7$ places a lower bound on the asymmetry parameter

$$\mathcal{A} \gtrsim 1 + \frac{0.49}{(1 - \mathcal{P}_{\text{macro}})^{4/3}} . \quad (19)$$

According to Equation (19), macroporosity $\mathcal{P}_{\text{macro}} > 0.9$ would require very extreme shapes with $\mathcal{A} \gtrsim 12$ (e.g., oblate spheroids with axial ratio exceeding $\sim 12:1$, or prolate spheroids with axial ratio exceeding $\sim 16:1$) to achieve $\Phi_{\text{PSA}} \gtrsim 0.7$ as required by observations. Such extreme shapes seem implausible.

8. POLARIZATION IN THE INFRARED

8.1. Far-Infrared

For a given grain shape, the polarization fraction of the FIR emission depends on the degree of alignment of the grains. For the degree of alignment that reproduces the observed maximum amount of starlight polarization per unit reddening, one can predict the maximum amount of FIR polarization, $[p_{\text{em}}(\text{FIR})]_{\text{max}}$. Because the fractional polarization is essentially independent of λ for $\lambda \gtrsim 50\mu\text{m}$ (see

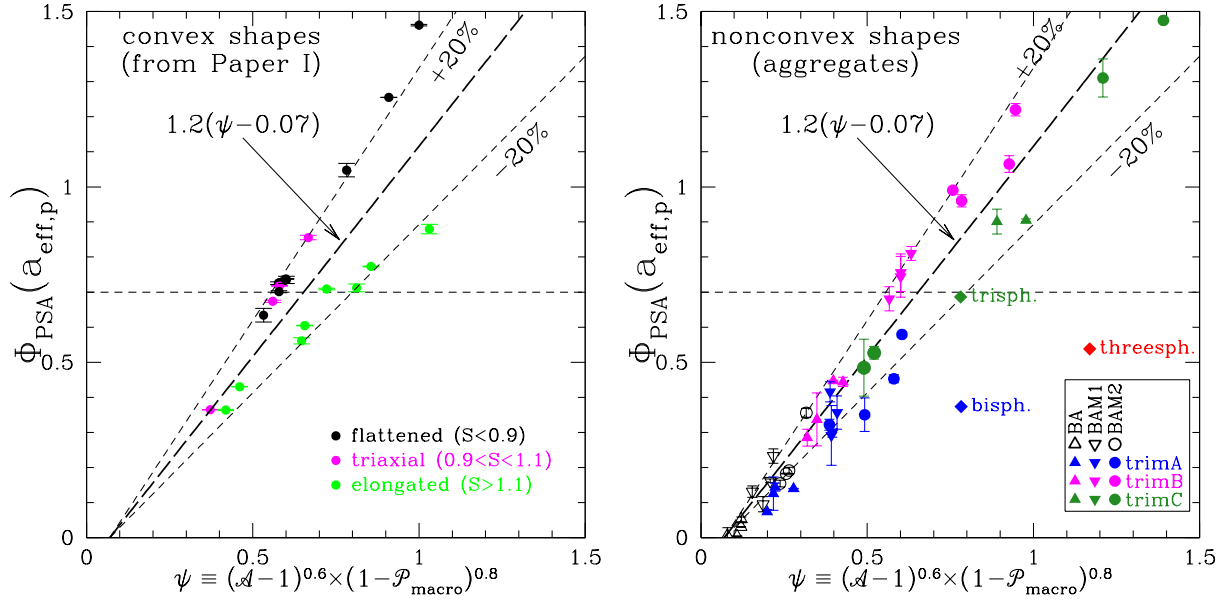


Figure 14. Starlight polarization efficiency factor Φ_{PSA} vs. $\psi \equiv (\mathcal{A} - 1)^{0.8} (1 - \mathcal{P}_{\text{macro}})^{0.6}$ for (a) convex shapes from Draine (2024) (b) nonconvex aggregates in present study.

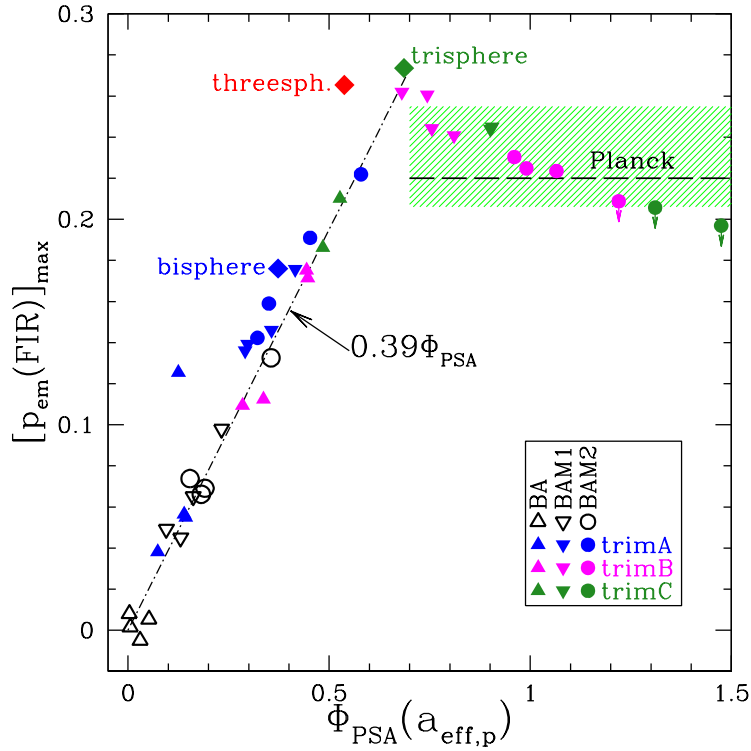


Figure 15. Polarization parameters $[p_{\text{em}}(\text{FIR})]_{\text{max}}$ and $\Phi_{\text{PSA}}(a_{\text{eff,p}})$ for the 45 aggregates. The region allowed by Planck polarization is shown in green. 7 shapes fall within the allowed region.

Fig. 11 of Paper I), we can compare the calculated maximum polarization fraction $[p_{\text{em}}(100\mu\text{m})]_{\text{max}}$ with $[p_{\text{em}}(850\mu\text{m})]_{\text{max}} = 0.220^{+0.035}_{-0.014}$ determined by [Planck Collaboration et al. \(2020\)](#).

Table 2 lists $[p_{\text{em}}(\text{FIR})]_{\text{max}}$ evaluated using Equation (28) from Paper I.⁹ Figure 15 shows $[p_{\text{em}}(\text{FIR})]_{\text{max}}$ versus $\Phi_{\text{PSA}}(a_{\text{eff,p}})$ for the 45 nonconvex shapes studied here. For $\Phi_{\text{PSA}}(a_{\text{eff,p}}) < 0.7$, $[p_{\text{em}}(\text{FIR})]_{\text{max}}$ varies approximately linearly with $\Phi_{\text{PSA}}(a_{\text{eff,p}})$ (dot-dash line in Figure 15).

The calculated values of $[p_{\text{em}}(\text{FIR})]_{\text{max}}$ are very small for the BA, BAM1, and BAM2 random aggregates, particularly the highest-porosity BA aggregates, but these shapes are already ruled out by their inability to provide enough starlight polarization. Figure 13 showed that 10 of the trimmed aggregates were consistent with starlight polarization, including the requirement $\sigma_p < 0.6$; Figure 15 shows that 7 of these are also consistent with the *Planck* polarization constraints.

It is also notable in Figure 15 that the 13 shapes with $\Phi_{\text{PSA}} > 0.65$ have $[p_{\text{em}}(\text{FIR})]_{\text{max}}$ tending to decline with increasing Φ_{PSA} : as the shapes become more asymmetric, the starlight polarization efficiency Φ_{PSA} increases more rapidly than $Q_{\text{pol,PSA}}/Q_{\text{ran}}$, resulting in a drop in $[p_{\text{em}}(\text{FIR})]_{\text{max}}$. The same trend was previously seen for prolate spheroids, oblate spheroids, and square prisms ([Draine 2024](#)). For all studied shapes (including the convex shapes in Paper I), we have no examples of shapes with $\Phi_{\text{PSA}} > 1.3$ that have $[p_{\text{em}}(\text{FIR})]_{\text{max}}$ large enough to be consistent with the *Planck* constraint.

It is important to note that the present results were all calculated using a single dielectric function. As discussed above, for the $M = 256$ aggregates, this dielectric function gives a FIR opacity exceeding the observed value (see Figures 8-11). A dielectric function with reduced FIR absorption (as required for these aggregates to be consistent with the observed FIR-submm opacity) would give less total emission and less polarized emission in the FIR. The reduction in both $\text{Re}(\epsilon)$ and $\text{Im}(\epsilon)$ will result in a modest reduction in the polarization fraction in the FIR.¹⁰ Allowing for this reduction in $[p_{\text{em}}(\text{FIR})]_{\text{max}}$, we conclude that the three shapes with $\Phi_{\text{PSA}} > 1.2$ fall below the allowed range of $[p_{\text{em}}(\text{FIR})]_{\text{max}}$: only seven of the 45 shapes considered here have $\Phi_{\text{PSA}} > 0.7$ and $[p_{\text{em}}(\text{FIR})]_{\text{max}}$ consistent with *Planck*.

8.2. $10\mu\text{m}$ Polarization

In the astrodust model ([Hensley & Draine 2023](#)), the grains providing starlight polarization are composed of a mixture of materials, including the amorphous silicates that produce infrared extinction. In this model, starlight polarization in the optical must be accompanied by polarization in the $10\mu\text{m}$ silicate feature. We calculate the ratio of the $10\mu\text{m}$ polarization cross section per unit volume to the starlight polarization efficiency integral $\Phi_{\text{PSA}}(a_{\text{eff,p}})$ following the treatment in Paper I.

The untrimmed BA, BAM1, and BAM2 random aggregates are not of interest: for these shapes, Φ_{PSA} is so small that such grains are incapable of contributing appreciably to the observed starlight polarization. In Figure 16 we show $C_{\text{pol,PSA}}(\lambda)/(V_{\text{solid}}\Phi_{\text{PSA}})$ for the trisphere geometry and examples of BAM1trimB and BAM1trimC aggregates that are compatible with starlight polarization, as well as a 5:7:7 oblate spheroid ([Draine 2024](#)). Table 3 lists results for the 7 aggregates that are compatible with starlight polarization and *Planck* polarization (see Figure 15). The $10\mu\text{m}$ polarization profile is nearly unaffected by shape or porosity.

Averaging the polarization from $10\mu\text{m}$ to $11\mu\text{m}$, all seven shapes fall in the relatively narrow range

$$\frac{\Delta C_{\text{pol,PSA}}(\text{sil.})}{V_{\text{solid}}\Phi_{\text{PSA}}} \equiv \frac{C_{\text{pol,PSA}}(10-11\mu\text{m}) - C_{\text{pol,PSA}}(8-9\mu\text{m})}{V_{\text{solid}}\Phi_{\text{PSA}}} = 1114 \pm 29 \text{ cm}^{-1} \quad . \quad (20)$$

⁹ For shapes with $\Phi_{\text{PSA}}(a_{\text{eff,p}}) < 0.7$ (35 of the 45 shapes in the present study), $[p_{\text{em}}(\text{FIR})]_{\text{max}}$ is evaluated assuming that a fraction $f_{\text{align}} = 0.7$ of the grain mass is in perfect spinning alignment, and the remaining 30% of the mass is in small grains that are randomly oriented. For shapes with $\Phi_{\text{PSA}}(a_{\text{eff,p}}) > 0.7$, $[p_{\text{em}}(\text{FIR})]_{\text{max}}$ is calculated assuming $f_{\text{align}} = 0.49/\Phi_{\text{PSA}}(a_{\text{eff,p}})$.

¹⁰ Figure 11 of Paper I shows the fractional polarization for 2:1 oblate spheroids calculated with two different dielectric functions. The change in dielectric function resulted in a drop in $[p_{\text{em}}(\text{FIR})]_{\text{max}}$ from 0.171 to 0.166 – a fractional reduction of $\sim 3\%$ in $[p_{\text{em}}(\text{FIR})]_{\text{max}}$.

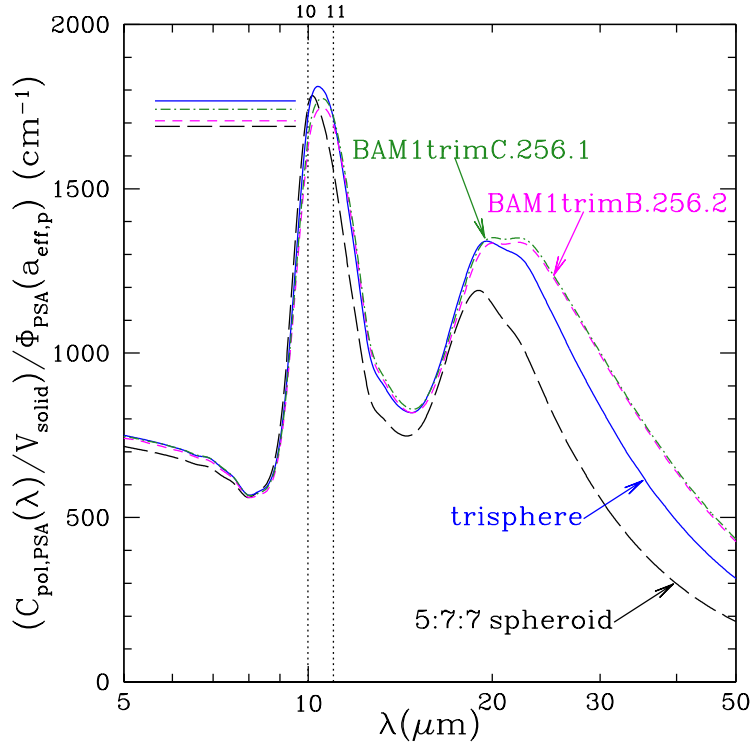


Figure 16. Polarization in the 10 and 18 μm silicate features relative to starlight polarization for three aggregates: the trisphere, BAM2trimB.256.1, and BAM2trimA.256.2. Result for 1.4:1 oblate spheroid is shown for comparison. Horizontal lines indicate values of $(\overline{C_{\text{pol,PSA}}(10 - 11\mu\text{m})}/V_{\text{solid}})/\Phi_{\text{PSA}}(a_{\text{eff,p}})$ (see Table 3).

This predicts polarization in the 10 μm feature, relative to the optical polarization p_{max} (Draine & Hensley 2021a; Draine 2024):

$$\begin{aligned} \left(\frac{\Delta p_{\text{sil}}}{p_{\text{max}}}\right) &= 1.23 \times 10^{-4} \text{ cm} \times \frac{\Delta C_{\text{pol,PSA}}(\text{sil.})}{V_{\text{solid}} \Phi_{\text{PSA}}} \\ &= 0.137 \pm 0.004 \quad . \end{aligned} \quad (21)$$

This will be further discussed in Section 9.3.

9. DISCUSSION

9.1. $N = 2$ and $N = 3$ Aggregates

Grain-grain collisions at speeds resulting in sticking are expected to take place in the ISM. Jura (1980) pointed out that coagulation appears to be *required* to explain the observed grain growth on the sightline to ρ Ophiuchi.

Coagulation of approximately equal-size grains might result in particles resembling the symmetric bisphere or trisphere geometries considered here. Prior to the present study, the symmetric bisphere geometry seemed likely (at least to the author) to be an efficient polarizer, at both optical and FIR wavelengths. It was anticipated that at optical wavelengths the same near-field wave effects that result in effective polarization by 2:1:1 prolate spheroids would make bispheres similarly effective.

Therefore, it was surprising to find that symmetric bispheres are significantly *less* effective for starlight polarization than 2:1:1 spheroids or 2:1:1 cylinders (see Figure 13), with $\Phi_{\text{PSA}}(a_{\text{eff,p}}) \approx 0.37$ – only $\sim 50\%$ of $\Phi_{\text{PSA}} \approx 0.7$ found in Paper I for 2:1:1 spheroids and 2:1:1 cylinders. The low polarizing

Table 3. 10 Micron Polarization

shape	$\mathcal{P}_{\text{macro}}$	Φ_{PSA}	$\left[\frac{C_{\text{pol,PSA}}(10-11 \mu\text{m})}{V_{\text{solid}} \Phi_{\text{PSA}}(a_{\text{eff,p}})} \right]$ (cm^{-1})	$\left[\frac{\Delta C_{\text{pol,PSA}}(\text{sil.})}{V_{\text{solid}} \Phi_{\text{PSA}}(a_{\text{eff,p}})} \right]$ (cm^{-1})
5:7:7 spheroid ^a	0.000	0.726 ± 0.004	1682 ± 1	1075 ± 3
BAM2trimB.256.1	0.584	0.991 ± 0.005	1707 ± 1	1103 ± 2
BAM2trimB.256.3	0.577	1.067 ± 0.022	1709 ± 6	1109 ± 7
BAM2trimB.256.4	0.591	0.961 ± 0.018	1702 ± 16	1101 ± 16
BAM1trimB.256.2	0.723	0.756 ± 0.054	1721 ± 9	1109 ± 11
BAM1trimB.256.3	0.690	0.811 ± 0.020	1741 ± 9	1129 ± 6
BAM1trimC.256.1	0.706	0.935 ± 0.026	1742 ± 10	1129 ± 9
BAM1trimC.256.2	0.727	0.905 ± 0.004	1749 ± 11	1131 ± 12
range for allowed aggregates			1733 ± 37	1114 ± 29

^a from Paper I (Draine 2024).

efficiency of bispheres implies that grains with bisphere morphology *cannot* contribute significantly to either the observed extinction curve or the observed starlight polarization.

Similarly, the $N = 3$ aggregates were expected to be effective polarizers. The trisphere and three-sphere structures both have starlight polarization efficiency factors Φ_{PSA} that are larger than the bisphere, but the threesphere geometry ($\Phi_{\text{PSA}} \approx 0.54$) still falls below the lower limit $\Phi_{\text{PSA}} > 0.7$ required to reproduce the observed polarization of starlight. The trisphere geometry, with $\Phi_{\text{PSA}} \approx 0.69$, is marginally compatible with starlight polarization.

A population of $N = 2$ and $N = 3$ aggregates would presumably include a substantial fraction of bispheres, and $N = 3$ shapes (e.g., the threesphere) that are less effective polarizers than the trisphere. Such a mixture would have $\langle \Phi_{\text{PSA}} \rangle$ well below the lower limit 0.7. We conclude that the observed starlight polarization cannot be accounted for by $N = 2$ and $N = 3$ aggregates of more-or-less spherical monomers.

9.2. FIR and Submm Polarization

The same grains that account for polarization of starlight must also reproduce the observed linear polarization of thermal emission from dust. At each point in the grain the local electric field is the sum of the incident wave plus radiation from other parts of the grain. In the optical, where starlight polarization peaks, the grain size a_{eff} is comparable to the wavelength λ , radiation arrives at different parts of the grain with different phase shifts, and interference effects are important. However, phase shifts are negligible at FIR wavelengths $\lambda \gg a_{\text{eff}}$. Thus, it was anticipated that the ratio of FIR polarization cross section to optical polarization cross section might be sensitive to both grain shape and porosity, so that measurement of polarization at both FIR and optical wavelengths might allow us to constrain the porosity.

In Paper I, which was limited to convex shapes with $\mathcal{P}_{\text{macro}} < 0.12$, it was found that all shapes which were compatible with the requirements $\Phi_{\text{PSA}} > 0.7$ and $\sigma_{\text{p}} \lesssim 0.6$ predicted maximum fractional polarization $[p_{\text{em}}(\text{FIR})]_{\text{max}}$ in the range 0.17-0.25, close to or within the *Planck* constraint $0.220^{+0.035}_{-0.014}$.

The present study has extended the calculations to irregular shapes with porosities $\mathcal{P}_{\text{macro}}$ up to 0.85. Seven of the BAM1trimB and BAM2trimB aggregates with $\Phi_{\text{PSA}} > 0.7$ have $[p_{\text{em}}(\text{FIR})]_{\text{max}}$ within the range allowed by *Planck*. We find that above the minimum value $\Phi_{\text{PSA}} = 0.7$ there appears to be a systematic trend for $[p_{\text{em}}(\text{FIR})]_{\text{max}}$ to decrease for increasing Φ_{PSA} : the three shapes with the largest Φ_{PSA} have $[p_{\text{em}}(\text{FIR})]_{\text{max}}$ below the range allowed by *Planck*. A similar trend was previously seen for prolate spheroids and oblate spheroids (see Figure 12b in Draine 2024). We conclude that if interstellar grains are porous aggregates with sufficient flattening or elongation to account for

the polarization, they will have $0.7 < \Phi_{\text{PSA}} \lesssim 1.2$, implying a relatively high fractional alignment $f_{\text{align}} \approx 0.7/\Phi_{\text{PSA}} \gtrsim 0.6$ for the $a_{\text{eff}} \gtrsim 0.05\mu\text{m}$ grains that account for more than 50% of the grain mass.

9.3. $10\mu\text{m}$ Polarization

The astroduct model – or any model which posits that one grain type dominates both starlight polarization and far-infrared emission – predicts that the silicate material in interstellar grains will produce polarization of starlight in the $10\mu\text{m}$ silicate feature, with $\Delta p(\text{sil}) \approx 0.137p_{\text{max}}$, where p_{max} is the polarization maximum (near $0.55\mu\text{m}$): see Equation (21). The only star where the optical polarization and the $10\mu\text{m}$ polarization have both been measured is the blue hypergiant Cyg OB2-12, where the optical polarization has $p_{\text{max}} = 0.0967 \pm 0.0010$ (Whittet et al. 1992) and the $10\mu\text{m}$ feature has excess polarization $\Delta p_{\text{sil}} \approx 0.0070 \pm 0.0035$ (Telesco et al. 2022). For Cyg OB2-12, the observed $\Delta p_{\text{sil}}/p_{\text{max}} = 0.072 \pm 0.036$ is $\sim 1.8\sigma$ lower than the value 0.137 predicted by Eq. (21).

The theoretical prediction (21) was found to be approximately independent of shape, for both the convex shapes in Paper I and the complex aggregate shapes studied here. Therefore, the discrepancy between the observed $\Delta p_{\text{sil}}/p_{\text{max}}$ and the prediction (Equation 21) cannot be attributed to uncertainties concerning the detailed shape of the grains providing the starlight polarization.

If the Telesco et al. (2022) result for $\Delta p_{\text{sil}}/p_{\text{max}}$ is confirmed, any grain model (e.g., the astroduct model) that posits a single grain component dominating both starlight polarization and far-infrared emission would appear to be ruled out. However, Draine (2024) has argued that Cyg OB2-12 may have significant *intrinsic* (apparently time-variable) polarization, complicating determination of the *interstellar* contribution to the polarization. More polarimetry of Cyg OB2-12 in the optical and mid-IR is needed to confirm the determination of $\Delta p_{\text{sil}}/p_{\text{max}}$ for interstellar dust. Studies of other sightlines are needed, to determine if this result is representative of the diffuse ISM.

9.4. Determination of Grain Porosities Using X-Rays

Small-angle scattering of X-rays by interstellar grains (Overbeck 1965) can provide an independent constraint on porosity. Suppose that dust is located on the path to a compact X-ray source, with d_s and d_X the distance from us to the dust and X-ray source, respectively. The halo angle $\theta_h \approx (1-\xi)\theta_s$, where θ_s is the scattering angle, and $\xi \equiv d_s/d_X < 1$.

At $E \gtrsim 1\text{keV}$ the scattering cross section $C_{\text{sca}} \propto a_{\text{eff}}^6$, and the scattering is dominated by the larger grains. The halo has a uniform surface brightness “core”, and extended wings with surface brightness $\propto \theta_s^{-4}$ (Draine 2003). The transition from core to wing takes place near the angle $\theta_{s,50} \approx \lambda/D_X$ containing 50% of the scattered power, where D_X is the characteristic diameter of the grains dominating the X-ray scattering.

For compact grains, the grain size distribution has $D_X \approx 0.6\mu\text{m}$, hence $\theta_{s,50} \approx 360''(\text{keV}/h\nu)$ (Draine 2003). If the grains are porous, we expect D_X to scale as D_p (see Eq. 14), i.e., $D_X \propto (1 - \mathcal{P}_{\text{macro}})^{-0.55}$. Thus we estimate

$$\theta_{s,50} \approx 360'' \left(\frac{\text{keV}}{h\nu} \right) (1 - \mathcal{P}_{\text{macro}})^{0.55} . \quad (22)$$

If the distribution of dust along the line-of-sight is known, then measurement of the dust-scattered halo can be used to constrain the porosities of interstellar grains.

The best measured X-ray halo is toward GX 13+1. Smith et al. (2002) and Smith (2008) found the observed $2'' < \theta_h < 900''$ X-ray halo to be generally consistent with models with compact grains, for uniform dust density along the path to the source, although the instrumental PSF dominates the observed halo profile for $\theta_h \lesssim 5''$. Smith et al. (2002) argued that highly porous grains (e.g., $\mathcal{P}_{\text{macro}} = 0.8$) were ruled out because they would produce insufficient X-ray scattering, but did not

allow for the increased size of the grains in such models as well as the nonuniform density within a grain with macroporosity.

Heng & Draine (2009) calculated X-ray scattering by BA, BAM1, and BAM2 aggregates. For equal-mass grains, increased porosity (BAM2→BAM1→BA) resulted in reduced $\theta_{s,50}$, as expected. Although computational limitations precluded use of realistic size distributions, Heng & Draine (2009) concluded that the observed X-ray halo around GX 13+1 was not consistent with random aggregates, while calling for more detailed modeling to confirm this.

With improved computational methods (Hoffman & Draine 2016), calculations of X-ray scattering for aggregates with size distributions that are compatible with interstellar reddening and polarization should now be feasible, enabling interstellar grain models with porous grains to be tested.

9.5. Implications for Grain Evolution

Grain growth by coagulation is expected to be important in the diffuse ISM. If we suppose that all of the grain mass is in spheres of mass-equivalent radius a_{eff} and density $\rho = \rho_{\text{solid}}(1 - \mathcal{P}_{\text{macro}})$, then in a region with H nucleon density n_{H} , the time for a grain to collide with an equal mass of dust (i.e., another grain) is

$$\tau_{\text{coll}} \approx \frac{1}{n_{\text{gr}} 4\pi a_{\text{eff}}^2 (1 - \mathcal{P}_{\text{macro}})^{-2/3} v_{\text{rel}}} \quad (23)$$

$$= 1.2 \times 10^7 \text{ yr} \left(\frac{a_{\text{eff}}}{0.2 \mu\text{m}} \right) \left(\frac{30 \text{ cm}^{-3}}{n_{\text{H}}} \right) \left(\frac{\text{km s}^{-1}}{v_{\text{rel}}} \right) \left(\frac{0.007}{Z_{\text{d}}} \right) (1 - \mathcal{P}_{\text{macro}})^{2/3}, \quad (24)$$

where v_{rel} is the characteristic grain-grain velocity, and Z_{d} is the mass fraction in dust. A more careful treatment would allow for a distribution of grain sizes, but (23) remains an informative estimate.

We consider a scenario where the large grains are aggregates of smaller particles of varied composition. In the diffuse ISM, grains are typically charged, and MHD turbulence is expected to result in $v_{\text{rel}} \approx 1 \text{ km s}^{-1}$ for grains with $a_{\text{eff}} \gtrsim 0.1 \mu\text{m}$ (Yan et al. 2004), with larger grains moving faster than smaller grains. For $v_{\text{rel}} \gtrsim 0.4 \text{ km s}^{-1}$, τ_{coll} is comparable to or shorter than the timescale $1/n_{\text{H}} R_{\text{H}_2}$ for conversion of H to H_2 by grain surface catalysis (for the empirical rate coefficient $R_{\text{H}_2} \approx 3 \times 10^{-17} \text{ cm}^3 \text{ s}^{-1}$; Jura 1975). Thus, the typical grain in molecular gas will have collided with several times its own mass of dust grains while the gas was converting from HI to H_2 .

Collisions between fast-moving large grains seem likely to result in shattering, particularly if one or both are aggregates; Yan et al. (2004) suggest that this may account for the sharp cutoff in the grain size distribution at $\sim 0.3 \mu\text{m}$, as well as replenishing the population of small grains. Grain growth may proceed by larger grains “sweeping up” smaller grains. When a very small grain ($a \lesssim 0.03 \mu\text{m}$) hits a much larger grain ($a \gtrsim 0.1 \mu\text{m}$) with an impact speed of $\sim 0.5 \text{ km s}^{-1}$, it seems possible that some impacts may result in the impactor sticking to or embedding itself within the larger grain, resulting in grain growth.

Coagulation acting alone will produce high-porosity aggregates resembling the BA, BAM1, or BAM2 structures, which we have seen above to be very weak polarizers, incompatible with the observed polarization of starlight and polarized far-infrared emission. There must be processes acting in the interstellar medium to increase the polarizing abilities of the aggregates, by reducing the porosity and/or increasing the asymmetry of the aggregates.

9.5.1. Densification by Crushing?

A porous grain undergoing a collision with another grain may undergo some degree of “crushing”, lowering the porosity. For aggregates of monodisperse SiO_2 spheres with initial porosities $\mathcal{P}_{\text{macro}} \approx 0.85$, Blum & Schr apler (2004) found that the porosity could be reduced to $\mathcal{P}_{\text{macro}} \approx 0.66$ if subjected

to a static pressure $p \approx 10^4$ dyne cm^{-2} . For initial porosities $\mathcal{P}_{\text{macro}} \approx 0.8$, simulations of aggregate-aggregate collisions with collision velocity 0.005 km s^{-1} resulted in partial fragmentation, but with a substantial fraction of the material remaining in a structure with lower porosity $\mathcal{P}_{\text{macro}} \approx 0.6$ (Gunkelmann et al. 2016; Planes et al. 2021). It seems plausible that continued aggregate-aggregate collisions with velocities in a suitable range might result in much of the mass residing in relatively compact aggregates, perhaps with porosities $\mathcal{P}_{\text{macro}} \lesssim 0.6$. However, based on our studies of BAM2 aggregates, even porosities $\mathcal{P}_{\text{macro}} \approx 0.6$ appear to be inconsistent with polarization observations, unless the structures are significantly more asymmetric than the BAM2 aggregates studied here.

9.5.2. Photolytic Densification?

In the diffuse ISM, the FUV intensity is such that a single electron in a chemical bond will be photoexcited to a higher energy orbital on a timescale of $\sim 10^{11}$ sec. Thus, on the $\sim 3 \times 10^8$ yr lifetime of a grain (e.g. Barlow 1978; Draine & Salpeter 1979a; Zhukovska et al. 2016; Hu et al. 2019), a single bonding electron will be photoexcited to a new electronic state $\sim 10^5$ times. If the new electronic state happens to be repulsive, an atom or radical may be displaced. It is conceivable that this process might result in a systematic tendency to reduce the porosity of the grain, with atoms or radicals gradually relocating to higher-coordination sites where they are more permanently bonded. Note that FUV photons can penetrate $\sim 0.1 \mu\text{m}$ into the grain, allowing this process to act even in the interior of a submicron aggregate.

Laboratory experiments on materials of technological interest for production of thin film transistors have demonstrated that some compounds can be “annealed” at room temperature if exposed to FUV radiation (e.g., Kim et al. 2012; Park et al. 2020). However, there do not appear to have been any laboratory studies of high-porosity materials to see whether densification occurs. Lab studies of FUV irradiation of silica aerogels would be valuable.

Cosmic rays are also important for exciting grain material, particularly the heavy ions (O^{+8} , Ne^{+10} , Fe^{+26}) (see, e.g., Leger et al. 1985). A low energy or high- Z cosmic ray passing through the grain leaves behind a hot channel which permits atomic rearrangement as the “thermal spike” cools by diffusion. The atomic rearrangement will tend to “anneal” the material, putting atoms into higher-coordination sites, reducing the spatial extent of the grain, and decreasing the porosity.

9.6. Processes that May Increase Grain Asymmetry

Growth by addition of single-size monomers produces aggregates resembling the BA, BAM1, or BAM2 structures, if the monomers stick at or close to the point of first contact.

However, grains in diffuse clouds with $a_{\text{eff}} \gtrsim 0.1 \mu\text{m}$ are expected to be spinning suprathermally, as the result of systematic torques resulting from photoelectron emission, H_2 formation, and starlight (Purcell 1975; Draine & Weingartner 1996); starlight torques are expected to dominate. In the diffuse ISM, $a_{\text{eff}} \approx 0.2 \mu\text{m}$ grains are expected to have rotation speeds $v_{\text{rot}} \lesssim 0.01 \text{ km s}^{-1}$ (Draine & Weingartner 1996), which seems too small to disrupt the grain,¹¹ but could conceivably affect the shape of the growing aggregate by favoring migration of weakly bound physisorbed atoms, molecules, or nanoparticles to locations near the “equator”. Higher rotation speeds occur for grains passing close to stars (see, e.g., Silsbee & Draine 2016; Hoang 2019), but such events are too rare to affect the overall grain population.

Significant asymmetry could result from coagulation of two already-large aggregates of comparable size, forming a bisphere-like geometry. However, we have seen that the bisphere produced by joining

¹¹ In a spinning solid sphere, the greatest stresses are near the center. The limiting equatorial speed is (Draine & Salpeter 1979b)

$$v_{\text{rot,max}} \approx c_s \times \left(\frac{S_{\text{yield}}}{Y} \right)^{1/2},$$

where Y is Young’s modulus, S_{yield} is the yield stress, and $c_s \approx (Y/\rho)^{1/2} \gtrsim 1 \text{ km s}^{-1}$ is the sound speed in the solid. For typical solids, $S_{\text{yield}} \gtrsim 0.01Y$, hence $v_{\text{rot,max}} \gtrsim 0.1c_s \approx 0.1 \text{ km s}^{-1}$

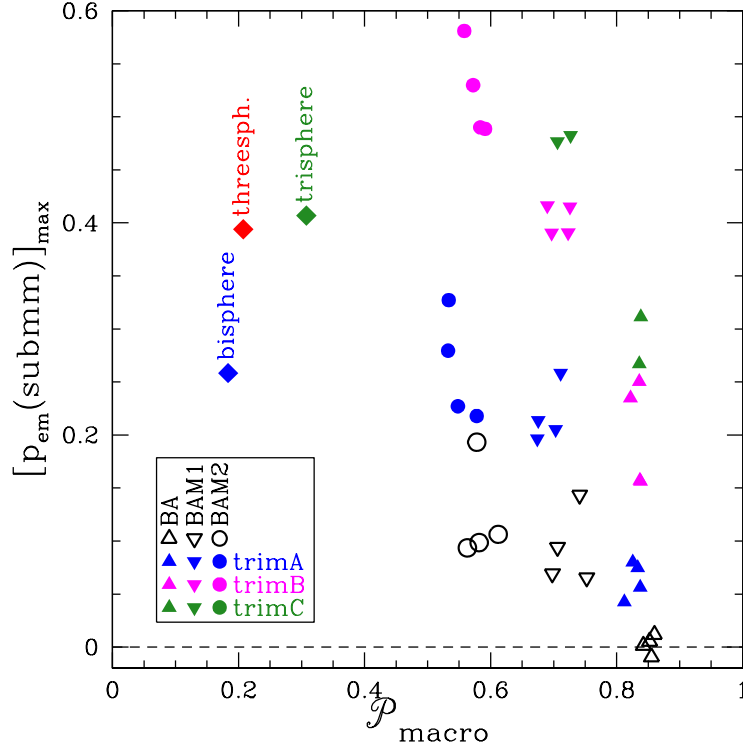


Figure 17. Maximum polarization of thermal emission for grains in the Rayleigh limit ($a_{\text{eff}} \lesssim \lambda/2\pi$) and perfect spinning alignment, versus macroporosity. The plain BA, BAM1, and BAM2 aggregates (open symbols) have $[p_{\text{em}}]_{\text{max}} < 0.20$. Polarizations exceeding 20% require that aggregate grains be densified or reshaped (see text).

together two $\mathcal{P}_{\text{macro}} = 0$ spheres has $\Phi_{\text{PSA}} = 0.37$, well below the $\Phi_{\text{PSA}} > 0.7$ required to explain the observed starlight polarization. Unless the two colliding aggregates fuse into a shape that is a significantly better polarizer than the bisphere, the final structure will have a low Φ_{PSA} .

If interstellar grains are high-porosity aggregates, there must be some mechanism to produce extreme asymmetries, e.g. $\mathcal{A} \gtrsim 3.4$ if $\mathcal{P}_{\text{macro}} \approx 0.7$ (see Equation 19). Suitable shapes can be obtained by systematically “trimming” initially random aggregates (e.g., the *trimB*, and *trimC* aggregates in Figures 5-6) but it is not clear what interstellar processes would impart such asymmetric shapes to porous aggregates. Atomic sputtering or grain-grain collisions can “trim” weakly-bound monomers from the surface, but the systematic effects on shape are unclear. The IDPs in Figure 1 are quite asymmetric, but the processes that shaped them remain unknown.

9.7. Grains in High Density Regions

Grain growth is seen in molecular clouds: changes in the extinction curve are observed, characterized by increases of $R_V \equiv A_V/E(B-V)$ from ~ 3.1 in the diffuse ISM to ~ 4.2 in the ρ Oph molecular cloud (Martin & Whittet 1990), and values as large as $R_V \approx 6$ in other clouds (Whittet 2022). Increased grain size is also revealed by increased scattering in the mid-infrared (“cloudshine” and “coreshine”) indicating growth of grains to radii $\sim 1.0\mu\text{m}$ in the externally illuminated regions of dense clouds (Foster & Goodman 2006; Paganì et al. 2010; Andersen et al. 2013; Steinacker et al. 2015).

The observed grain growth must be due to coagulation, and is presumably more advanced in denser regions. For grains in the Rayleigh limit $a_{\text{eff}} \ll \lambda$, Figure 17 shows the maximum possible polarization at mm and submm wavelengths, for grains in perfect spinning alignment. Plain BA, BAM1, or BAM2 coagulation results in porous aggregates that are poor polarizers. Therefore, one might have expected lower fractional polarization of submm emission in high column density regions.

BLASTPol observations of emission from dust in the Vela C molecular cloud (Fissel et al. 2016) found that the fractional polarization decreases with increasing column density. Fissel et al. (2016) concluded that even after allowing for magnetic field disorder, the observations suggest that dust in denser regions is less effective at producing polarization than dust in diffuse regions.

However, Le Gouellec et al. (2020) analyzed ALMA observations of 12 nearby low- and intermediate-mass Class 0 protostellar cores, and concluded that observed reductions in fractional polarization may be primarily due to magnetic field disorder, with no evidence of reductions in polarizing ability due to reduced degree of grain alignment. The low-mass Class 0 protostellar core NGC 1333 IRAS4A1 is a conspicuous example: at $870\mu\text{m}$, regions ~ 400 AU NE and ~ 400 AU SW of IRAS4A1 have polarization fractions exceeding 20%, with a similar polarization fraction at 6.9 mm (Ko et al. 2020). The dust at these locations must have a submm polarizing efficiency comparable to dust in the diffuse ISM. If, as expected, the dust particles have grown by coagulation, there must be processes acting to increase the flattening or elongation of the aggregates, and/or reduce their porosity, even in these dense regions.

10. SUMMARY

The principal results are as follows:

1. The grains producing the observed polarization of starlight cannot resemble bispheres: they are too inefficient as polarizers, and therefore cannot be common in the interstellar grain population.
2. The observed polarizing properties of interstellar dust cannot be accounted for by mixtures of $N = 2$ and $N = 3$ aggregates of more-or-less spherical monomers.
3. The empirical scaling relation (17) can be used to estimate Φ_{PSA} from the porosity $\mathcal{P}_{\text{macro}}$ and asymmetry parameter \mathcal{A} .
4. If interstellar grains have high porosity, they must also be extremely flattened or elongated in order to reproduce polarization observations. Porosity $\mathcal{P}_{\text{macro}} = 0.90$ requires $\mathcal{A} \gtrsim 12$. Unless there is a process to produce very extreme aspect ratios, porosities $\mathcal{P}_{\text{macro}} \gtrsim 0.90$ are ruled out by starlight polarization.
5. Seven of the *trimB* and *trimC* aggregates studied are consistent with starlight polarization ($\Phi_{\text{PSA}} > 0.7$) and the submm polarization fraction observed by *Planck*. All have $\mathcal{P}_{\text{macro}} < 0.73$, and $\Phi_{\text{PSA}} < 1.2$.
6. All shapes that are able to reproduce the starlight polarization have similar $[\Delta C_{\text{pol,PSA}}(\text{sil})/V]/\Phi_{\text{PSA}}$, where $\Delta C_{\text{pol,PSA}}(\text{sil})$ is the polarization cross section due to the $10\mu\text{m}$ silicate feature. The different shapes, therefore, predict similar ratios $\Delta p(\text{sil})/p_{\text{max}}$, where p_{max} is the peak starlight polarization, and $\Delta p(\text{sil})$ is the polarization due to the silicate feature.
7. The discrepancy between the predicted (Draine & Hensley 2021a) and observed (Telesco et al. 2022) $10\mu\text{m}$ polarization of Cyg OB2-12 is not resolved by varying the assumed grain shape. If the measurement by Telesco et al. (2022) is confirmed to characterize interstellar dust, the astro dust model (positing a single dominant grain type) will be disfavored. However, because Cyg OB2-12 itself appears to have time-variable intrinsic polarization, the ratio $\Delta p(\text{sil})/p_{\text{max}}$ should be measured on other sightlines.
8. X-ray scattering can be used to constrain grain porosities. The observed X-ray scattering halo around GX 13+1 may rule out models with $\mathcal{P}_{\text{macro}} > 0.55$ (Heng & Draine 2009), but more extensive modeling is required to confirm this.

9. Random coagulation acting alone would result in high porosities and modest overall asymmetries that together are incompatible with the observed polarization of starlight and polarized FIR emission. Because coagulation is expected, the observed polarization requires processes that (1) increase the elongation or flattening and/or (2) reduce the porosity. Crushing (during grain-grain collisions) can reduce the porosities of aggregates that are not disrupted.
10. The FUV radiation in diffuse clouds may lead to reduction in porosity through “photolytic densification”. Transient ionization and heating by cosmic rays may also contribute to densification. Even in the presence of grain growth by coagulation, photolytic densification may keep grain porosity low, so that interstellar polarization can be explained by axial ratios that are not extreme.
11. The polarized emission observed in some Class 0 cores, with fractional polarization $p > 20\%$, implies that grain growth in dense clouds must be accompanied by processes that either reduce the porosity or enhance the shape asymmetry.

1 I thank Don Brownlee, Henner Busemann, and Nicole Spring for permission to use the images
 2 in Figure 1. I thank Massimo Bertini, Larry Nittler and Rhonda Stroud for helpful discussions,
 3 and Robert Lupton for availability of the SM package. I thank the anonymous referee for helpful
 4 suggestions that improved the manuscript. I gratefully acknowledge support from NFS grant AST-
 5 1908123, and from the Institute for Advanced Study.

REFERENCES

- Andersen, M., Steinacker, J., Thi, W.-F., et al. 2013, *A&A*, 559, A60, doi: [10.1051/0004-6361/201322102](https://doi.org/10.1051/0004-6361/201322102)
- Barlow, M. J. 1978, *MNRAS*, 183, 367
- Beckwith, S. V. W., & Sargent, A. I. 1991, *ApJ*, 381, 250, doi: [10.1086/170646](https://doi.org/10.1086/170646)
- Blum, J., & Schr ppler, R. 2004, *PhRvL*, 93, 115503, doi: [10.1103/PhysRevLett.93.115503](https://doi.org/10.1103/PhysRevLett.93.115503)
- Bradley, J. P. 2003, *Treatise on Geochemistry*, 1, 711, doi: [10.1016/B0-08-043751-6/01152-X](https://doi.org/10.1016/B0-08-043751-6/01152-X)
- Draine, B. T. 2003, *ApJ*, 598, 1026, doi: [10.1086/379123](https://doi.org/10.1086/379123)
- . 2006, *ApJ*, 636, 1114, doi: [10.1086/498130](https://doi.org/10.1086/498130)
- . 2024, *ApJ*, accepted; arXiv:2310.15229
- Draine, B. T., & Flatau, P. J. 1994, *J. Opt. Soc. Am. A*, 11, 1491, doi: [10.1364/JOSAA.11.001491](https://doi.org/10.1364/JOSAA.11.001491)
- Draine, B. T., & Fraise, A. A. 2009, *ApJ*, 696, 1, doi: [10.1088/0004-637X/696/1/1](https://doi.org/10.1088/0004-637X/696/1/1)
- Draine, B. T., & Hensley, B. S. 2021a, *ApJ*, 919, 65, doi: [10.3847/1538-4357/ac0050](https://doi.org/10.3847/1538-4357/ac0050)
- . 2021b, *ApJ*, 909, 94, doi: [10.3847/1538-4357/abd6c6](https://doi.org/10.3847/1538-4357/abd6c6)
- . 2021c, *ApJ*, 910, 47
- Draine, B. T., & Salpeter, E. E. 1979a, *ApJ*, 231, 438, doi: [10.1086/157206](https://doi.org/10.1086/157206)
- . 1979b, *ApJ*, 231, 77, doi: [10.1086/157165](https://doi.org/10.1086/157165)
- Draine, B. T., & Weingartner, J. C. 1996, *ApJ*, 470, 551, doi: [10.1086/177887](https://doi.org/10.1086/177887)
- Dwek, E. 1997, *ApJ*, 484, 779, doi: [10.1086/304370](https://doi.org/10.1086/304370)
- Fanciullo, L., Guillet, V., Boulanger, F., & Jones, A. P. 2017, *A&A*, 602, A7, doi: [10.1051/0004-6361/201630373](https://doi.org/10.1051/0004-6361/201630373)
- Fissel, L. M., Ade, P. A. R., Angil , F. E., et al. 2016, *ApJ*, 824, 134, doi: [10.3847/0004-637X/824/2/134](https://doi.org/10.3847/0004-637X/824/2/134)
- Foster, J. B., & Goodman, A. A. 2006, *ApJL*, 636, L105, doi: [10.1086/500131](https://doi.org/10.1086/500131)
- Gauss, C. F. 1831, cited in Wikipedia: Close packing of equal spheres
- Goodman, J., Draine, B. T., & Flatau, P. J. 1991, *Optics Letters*, 16, 1198, doi: [10.1364/OL.16.001198](https://doi.org/10.1364/OL.16.001198)
- Graham, J. R., Kalas, P. G., & Matthews, B. C. 2007, *ApJ*, 654, 595, doi: [10.1086/509318](https://doi.org/10.1086/509318)
- Gunkelmann, N., Ringl, C., & Urbassek, H. M. 2016, *A&A*, 589, A30, doi: [10.1051/0004-6361/201628081](https://doi.org/10.1051/0004-6361/201628081)
- Heng, K., & Draine, B. T. 2009, ArXiv:0906.0773

- Hensley, B. S., & Draine, B. T. 2021, *ApJ*, 906, 73, doi: [10.3847/1538-4357/abc8f1](https://doi.org/10.3847/1538-4357/abc8f1)
- . 2023, *ApJ*, 948, 55, doi: [10.3847/1538-4357/acc4c2](https://doi.org/10.3847/1538-4357/acc4c2)
- Hirashita, H., Il'in, V. B., Pagani, L., & Lefèvre, C. 2021, *MNRAS*, 502, 15, doi: [10.1093/mnras/staa4018](https://doi.org/10.1093/mnras/staa4018)
- Hoang, T. 2019, *ApJ*, 876, 13, doi: [10.3847/1538-4357/ab1075](https://doi.org/10.3847/1538-4357/ab1075)
- Hoffman, J., & Draine, B. T. 2016, *ApJ*, 817, 139, doi: [10.3847/0004-637X/817/2/139](https://doi.org/10.3847/0004-637X/817/2/139)
- Hu, C.-Y., Zhukovska, S., Somerville, R. S., & Naab, T. 2019, *MNRAS*, 487, 3252, doi: [10.1093/mnras/stz1481](https://doi.org/10.1093/mnras/stz1481)
- Jura, M. 1975, *ApJ*, 197, 575, doi: [10.1086/153545](https://doi.org/10.1086/153545)
- . 1980, *ApJ*, 235, 63, doi: [10.1086/157610](https://doi.org/10.1086/157610)
- Keller, L. P., & Messenger, S. 2005, in *Astronomical Society of the Pacific Conference Series*, Vol. 341, *Chondrites and the Protoplanetary Disk*, ed. A. N. Krot, E. R. D. Scott, & B. Reipurth, 657
- Kim, S.-H., & Martin, P. G. 1995, *ApJ*, 444, 293, doi: [10.1086/175604](https://doi.org/10.1086/175604)
- Kim, Y.-H., Heo, J.-S., Kim, T.-H., et al. 2012, *Nature*, 489, 128, doi: [10.1038/nature11434](https://doi.org/10.1038/nature11434)
- Ko, C.-L., Liu, H. B., Lai, S.-P., et al. 2020, *ApJ*, 889, 172, doi: [10.3847/1538-4357/ab5e79](https://doi.org/10.3847/1538-4357/ab5e79)
- Le Gouellec, V. J. M., Maury, A. J., Guillet, V., et al. 2020, *A&A*, 644, A11, doi: [10.1051/0004-6361/202038404](https://doi.org/10.1051/0004-6361/202038404)
- Leger, A., Jura, M., & Omont, A. 1985, *A&A*, 144, 147
- Li, A. 2005, *ApJ*, 622, 965, doi: [10.1086/428038](https://doi.org/10.1086/428038)
- Martin, P. G., & Whittet, D. C. B. 1990, *ApJ*, 357, 113, doi: [10.1086/168896](https://doi.org/10.1086/168896)
- Mathis, J. S. 1996, *ApJ*, 472, 643, doi: [10.1086/178094](https://doi.org/10.1086/178094)
- Mathis, J. S., Rumpl, W., & Nordsieck, K. H. 1977, *ApJ*, 217, 425
- Mathis, J. S., & Whiffen, G. 1989, *ApJ*, 341, 808, doi: [10.1086/167538](https://doi.org/10.1086/167538)
- Mukai, T., Ishimoto, H., Kozasa, T., Blum, J., & Greenberg, J. M. 1992, *A&A*, 262, 315
- Ossenkopf, V. 1993, *A&A*, 280, 617
- Overbeck, J. W. 1965, *ApJ*, 141, 864, doi: [10.1086/148180](https://doi.org/10.1086/148180)
- Pagani, L., Steinacker, J., Bacmann, A., Stutz, A., & Henning, T. 2010, *Science*, 329, 1622, doi: [10.1126/science.1193211](https://doi.org/10.1126/science.1193211)
- Park, J. W., Kang, B. H., & Kim, H. J. 2020, *Advanced Functional Materials*, 30, 1904632, doi: [10.1002/adfm.201904632](https://doi.org/10.1002/adfm.201904632)
- Planck Collaboration, Aghanim, N., Akrami, Y., et al. 2020, *A&A*, 641, A12, doi: [10.1051/0004-6361/201833885](https://doi.org/10.1051/0004-6361/201833885)
- Planes, M. B., Millán, E. N., Urbassek, H. M., & Bringa, E. M. 2021, *MNRAS*, 503, 1717, doi: [10.1093/mnras/stab610](https://doi.org/10.1093/mnras/stab610)
- Purcell, E. M. 1975, in *The Dusty Universe*, ed. G. B. Field & A. G. W. Cameron (New York: Neale Watson Academic), 155–167
- Robertson, J. 1986, *Advances in Physics*, 35, 317, doi: [10.1080/00018738600101911](https://doi.org/10.1080/00018738600101911)
- Rogers, C., & Martin, P. G. 1979, *ApJ*, 228, 450, doi: [10.1086/156866](https://doi.org/10.1086/156866)
- Shen, Y., Draine, B. T., & Johnson, E. T. 2008, *ApJ*, 689, 260, doi: [10.1086/592765](https://doi.org/10.1086/592765)
- . 2009, *ApJ*, 696, 2126, doi: [10.1088/0004-637X/696/2/2126](https://doi.org/10.1088/0004-637X/696/2/2126)
- Silsbee, K., & Draine, B. T. 2016, *ApJ*, 818, 133, doi: [10.3847/0004-637X/818/2/133](https://doi.org/10.3847/0004-637X/818/2/133)
- Smith, R. K. 2008, *ApJ*, 681, 343, doi: [10.1086/588519](https://doi.org/10.1086/588519)
- Smith, R. K., Edgar, R. J., & Shafer, R. A. 2002, *ApJ*, 581, 562, doi: [10.1086/344151](https://doi.org/10.1086/344151)
- Steinacker, J., Andersen, M., Thi, W.-F., et al. 2015, *A&A*, 582, A70, doi: [10.1051/0004-6361/201425434](https://doi.org/10.1051/0004-6361/201425434)
- Telesco, C. M., Varosi, F., Wright, C., et al. 2022, *ApJL*, 940, L26, doi: [10.3847/2041-8213/ac9b56](https://doi.org/10.3847/2041-8213/ac9b56)
- Testi, L., Natta, A., Shepherd, D. S., & Wilner, D. J. 2003, *A&A*, 403, 323, doi: [10.1051/0004-6361:20030362](https://doi.org/10.1051/0004-6361:20030362)
- Voshchinnikov, N. V., Il'in, V. B., Henning, T., & Dubkova, D. N. 2006, *A&A*, 445, 167, doi: [10.1051/0004-6361:20053371](https://doi.org/10.1051/0004-6361:20053371)
- Whittet, D. C. B. 2022, *Dust in the Galactic Environment (Third Edition)*, 2514-3433 (Bristol: IOP Publishing), doi: [10.1088/2514-3433/ac7204](https://doi.org/10.1088/2514-3433/ac7204)
- Whittet, D. C. B., Martin, P. G., Hough, J. H., et al. 1992, *ApJ*, 386, 562, doi: [10.1086/171039](https://doi.org/10.1086/171039)
- Witten, T. A., & Cates, M. E. 1986, *Science*, 232, 1607, doi: [10.1126/science.232.4758.1607](https://doi.org/10.1126/science.232.4758.1607)
- Yajima, S., Satow, T., & Hirai, T. 1965, *Journal of Nuclear Materials*, 17, 127, doi: [10.1016/0022-3115\(65\)90029-2](https://doi.org/10.1016/0022-3115(65)90029-2)
- Yan, H., Lazarian, A., & Draine, B. T. 2004, *ApJ*, 616, 895, doi: [10.1086/425111](https://doi.org/10.1086/425111)

Ysard, N., Jones, A. P., Guillet, V., et al. 2024,

arXiv e-prints, arXiv:2401.07739,

doi: [10.48550/arXiv.2401.07739](https://doi.org/10.48550/arXiv.2401.07739)

Zhang, S., Zhu, Z., Ueda, T., et al. 2023, arXiv

e-prints, arXiv:2306.00158,

doi: [10.48550/arXiv.2306.00158](https://doi.org/10.48550/arXiv.2306.00158)

Zhukovska, S., Dobbs, C., Jenkins, E. B., &

Klessen, R. S. 2016, ApJ, 831, 147,

doi: [10.3847/0004-637X/831/2/147](https://doi.org/10.3847/0004-637X/831/2/147)

APPENDIX

A. COMPUTATIONAL DETAILS

The computations were carried out using the DDA code DDSCAT 7.3.3,⁸ with error tolerance $TOL = 1 \times 10^{-5}$. The numbers of dipoles N_1 , N_2 , N_3 used for the different target realizations are listed in Table 4. In Paper I, it was feasible to carry out calculations with much larger values of N_1, N_2, N_3 than for the BA, BAM1, and BAM2 aggregates in the present study, because:

1. The symmetries of the convex targets considered in Paper I meant that fewer target orientations were needed than for the asymmetric BA, BAM1, and BAM2 targets (e.g., for the cylindrical targets in paper I, only 11 orientations were needed, vs. the $12 \times 11 = 132$ orientations used for the BA, BAM1, and BAM2 targets).
2. The FFT methodology (Goodman et al. 1991) employed in DDSCAT requires a rectangular “computational volume” that contains all occupied lattice sites. For porous structures, the many unoccupied lattice sites within this computational volume impose a computational burden, which limits us to relatively modest numbers of occupied lattice sites N_1 in the largest calculations for the BA, BAM1, and BAM2 targets.

Because the number of dipoles per spherical monomer is not very large (e.g., $209917/256 \approx 820$ for the BA.256.2 target), the discreteness leads to limited fidelity in the calculated cross sections for the N_1, N_2, N_3 values used. As a result, the extrapolation procedure has relatively large uncertainties, particularly for the BA aggregates.

In all cases our uncertainty estimates are based on the difference between extrapolation using (N_1, N_2) and extrapolation using (N_2, N_3) and Equation (9) from Draine (2024). We do not include uncertainties resulting from the use of a finite number of target orientations, or due to use of a finite number of wavelengths in evaluation of the integral (16) for Φ_{PSA} .

B. SUPPLEMENTARY MATERIAL

Supplementary material, including images of all of the targets, parameter files (`ddscat.par`), as well as files specifying the target geometries and dielectric function used in this study are available at http://www.astro.princeton.edu/~draine/Draine_2024b_suppmat.html.

Table 4. Numbers of Dipoles Employed

shape	N_1	N_2	N_3
bisphere	2209298	769872	277968
threesphere	198608	102072	52264
trisphere	2748360	1411420	421408
BA.256.1	264622	135950	78757
BA.256.2	209917	132484	76821
BA.256.3	263017	165792	96341
BA.256.4	275676	201131	141494
BAM1.256.1	377960	115481	28326
BAM1.256.2	281493	197919	114873
BAM1.256.3	297503	172632	88663
BAM1.256.4	268258	188641	109439
BAM2.256.1	262890	135198	57378
BAM2.256.2	319152	185369	95081
BAM2.256.3	358900	208132	107021
BAM2.256.4	249256	144616	74337
BAttrimA.256.1	110338	56820	24101
BAttrimA.256.2	61569	26179	15265
BAttrimA.256.3	70907	41301	21273
BAttrimA.256.4	50582	29359	15075
BAM1trimA.256.1	231109	99109	57035
BAM1trimA.256.2	216688	111419	45154
BAM1trimA.256.3	58951	34288	17635
BAM1trimA.256.4	50304	29192	15077
BAM2trimA.256.1	137087	79709	41207
BAM2trimA.256.2	153420	65103	37800
BAM2trimA.256.3	106205	61793	31709
BAM2trimA.256.4	49195	25421	13129
BAttrimB.256.1	218532	126830	65153
BAttrimB.256.2	91070	43515	22375
BAttrimB.256.3	69764	35993	18595
BAttrimB.256.4	55960	32387	16668
BAM1trimB.256.1	148098	86079	44388
BAM1trimB.256.2	147799	85718	44124
BAM1trimB.256.3	96774	41132	23895
BAM1trimB.256.4	108484	62895	32376
BAM2trimB.256.1	231236	119352	61683
BAM2trimB.256.2	178617	125619	72935
BAM2trimB.256.3	55163	23504	12255
BAM2trimB.256.4	51260	29865	15372
BAttrimC.256.1	57004	33137	17189
BAttrimC.256.2	60067	34836	17903
BAM1trimC.256.1	70905	30045	17486
BAM1trimC.256.2	87606	45078	19164
BAM2trimC.256.1	77192	32730	18954
BAM2trimC.256.2	75871	32110	18592